UNIVERSITY OF OKLAHOMA

GRADUATE COLLEGE

OBJECTIVE CHARACTERIZATION OF IN-LINE PHASE CONTRAST X-RAY IMAGING PROTOTYPE USING A MID-ENERGY BEAM

A THESIS

SUBMITTED TO THE GRADUATE FACULTY

In partial fulfillment of the requirements for the

Degree of

MASTER OF SCIENCE

BY

BRADLEY GREGORY

Norman, Oklahoma

2019

OBJECTIVE CHARACTERIZATION OF IN-LINE PHASE CONTRAST X-RAY IMAGING PROTOTYPE USING A MID-ENERGY BEAM

A THESIS APPROVED FOR THE

SCHOOL OF ELECTRICAL AND COMPUTER ENGINEERING

BY

Dr. Hong Liu, Chair

Dr. Bin Zheng

Dr. Joseph Havlicek

Acknowledgements

I would like to extend my gratitude to Dr. Liu for giving me the opportunity to conduct research as a part of his lab group. I have learned much about research and scholarly writing and will undoubtedly apply what I have learned for many years to come. I would also like to acknowledge Dr. Yuhua Li, Dr. Muhammad Ghani, and Farid Omoumi for all their help in planning and conducting this investigation. As I struggled to adjust to a new normal after the loss of my father this past January, their help and guidance in the lab helped make life a little easier.

I would also like to thank Dr. Bin Zheng and Dr. Joseph Havlicek for agreeing to serve on my thesis committee.

This thesis is dedicated in loving memory of my father, Paul Gregory, whose perseverance, love, and kindness in life continue to ground and inspire me every day. This thesis is also dedicated to my mother, Lisa Gregory, whose strength, love, and determination have rescued me innumerable times while on this journey.

Table of Contents

List of Tables

List of Figures

Abstract

The purpose of the research presented in this thesis is the characterization of an in-line phase contrast x-ray imaging prototype operating at mid-energy, and to compare the data to that of high energy imaging with the same prototype. The prototype of interest has already been well characterized for high energy in-line phase contrast imaging. High energy imaging was the primary research focus for this prototype because a technique called phase retrieval required high energy phase contrast images to be implemented properly. Phase retrieval recovers a map of the phase shifts detected within a phase contrast image. The phase retrieval algorithm used by partners of this lab group has historically relied on high energy imaging due to its dependence on the phenomenon known as phase-attenuation duality. That algorithm is now under development for mid-energy x-ray imaging as well. Though this research does not involve phase retrieval directly, it is still necessary to characterize the prototype for mid-energy phase contrast imaging, before phase retrieval at mid-energy can be evaluated. The research presented in this thesis involved investigations into three image quality metrics. First, images taken of an edge device were taken to calculate the modulation transfer function. An angle resolution pattern device was then imaged to corroborate the cutoff frequency indicated by the first study. Images were then obtained with no object but with a virtual detector to calculate the noise power spectrum. Finally, the first and second studies' results were used to calculate the detective quantum efficiency of the prototype system. The study focused on images obtained with a source potential of 60kV, the results from which were compared to those from images obtained with

source potentials of 90kV and 120kV. A micro focus x-ray source was used with a CMOS based flat panel detector. The source-to-object and source-to-image distances were set such that a magnification of 2.2 was introduced. Results indicate that the prototype system's detective quantum efficiency at 60kVp was higher than it was for 90kVp and 120kVp. The mid-energy phase contrast imaging technique has potential for offering high detectability with lower dose to a patient for applications such as breast cancer diagnosis, as compared to current, conventional mammographic procedures.

Chapter 1. Introduction

1.1 Importance of Early Detection

In the United States, cancer is the second leading cause of death, only superseded by cardiovascular disease [1]. In 2019, it is estimated that 606,880 men and women will die due to cancer, while 1,762,450 are expected to be diagnosed with some form of the disease [2]. Early detection due to regular screening is therefore important to the improvement of survivability in patients [3, 4]. Breast cancer is among the most common forms, representing approximately 30 per cent of new cases expected in women for 2019 [2]. Mammography is an important key to early breast cancer detection. The procedure's success in reducing mortality has been well documented in the decades since its introduction [5-8]. There are some risks associated with mammography (and indeed all x-ray-based imaging procedures) stemming from exposure to x-rays, which are an ionizing form of electromagnetic radiation. Regulation helps to mitigate the risk by limiting the dosage a patient may receive for certain procedures and over certain periods of time and determining who may undergo those procedures. Nevertheless, there will always be some increased risk of carcinogenesis whenever x-ray images are taken [9]. It is therefore imperative to find an optimal balance between dose and x-ray image quality.

Since the early days of x-ray diagnostic imaging, conventional radiographic procedures have relied on the attenuation of x-ray beams due to absorption and scattering to capture the desired image. Attenuation coefficients vary between types of soft tissue. Glandular tissue, wherein neoplasms such as breast cancer commonly form, has a relatively high attenuation

coefficient compared to that of fat [10]. This difference in attenuation experienced by x-ray beams, makes glandular tissue easy to distinguish from the surrounding fat, as in the case of breast cancer. Unfortunately, there is no significant relative difference between the attenuation coefficients of malignant and benign glandular tissue [11]. While it is still possible to distinguish malignant and benign tissues, it can be difficult to do so.

Phase sensitive x-ray imaging, an emerging technology, shows promise in improving the distinguishability between malignant and benign tissue. It takes advantage of the x-ray beam's phase shift as well as the attenuation it experiences as the photons pass through soft tissue [12]. Whenever x-rays refract while passing through human tissues, they inevitably experience a phase shift. The phase-attenuation coefficient of human tissues has been determined to be greater than the linear attenuation coefficient by a factor of approximately 1000 [13]. At such a scale, any differences in phase shift between malignant and benign tissue will be much larger than differences in attenuation. The use of phase and attenuation information allows for improvements in image quality [14], and thus higher efficacy for the same radiation dose as that used in conventional radiography.

1.2 Research Goal

In-line phase contrast imaging is one technique used to implement phase sensitive x-ray imaging [15]. Systems used for this technique are designed similarly to conventional radiographic machines used today, but with a key difference: there is an "air gap" between the imaged object and the detector. This gap helps reduce scatter and increases interference between x-ray photons which have experienced different phase shifts, and thus enhance the edge between different tissues in an image [16-18]. The distance

between the object and detector also causes a magnification of the object in the image. The edge enhancement, reduction in scatter, and magnification can help a radiologist better distinguish between benign tissue and malignant neoplasms and do so more effectively than they would with conventionally obtained images with the same dose. To maximize the benefit from in-line phase contrast, it is necessary to extract the phase map from the image, a technique referred to as phase retrieval [19]. Until recently, the phase retrieval algorithm developed by Wu and Yan has been intended only for high energy images [12, 20, 21]. Today, the algorithm is being developed to be applied to mid-energy images. This thesis covers a characterization study for our prototype in-line phase contrast x-ray imaging system.

The purpose of the research is to examine the system's performance when obtaining phase contrast images with a source potential of 60kV and compare it to the system's performance when imaging with a high source potential (specifically 90kV and 120kV). For each energy setting, the modulation transfer function (MTF), noise power spectrum (NPS), and detective quantum efficiency (DQE) were calculated and compared to the others. An edge device, assembled in-lab, was used to calculate the MTFs for the single-projection study. The device and detector were aligned on an optical rail, and the source-to-object distance (SOD) and source-to-image distance (SID) were set such that the object was magnified in the image by a factor of 2.2. Images were also obtained of an angle resolution pattern, with the same SOD and SID, to confirm the cutoff spatial frequency indicated in the MTF calculations.

1.3 Organization of this Thesis

This thesis' organization is described as follows: Chapter 2 presents an overview of conventional, attenuation-based x-ray imaging theory. Chapter 3 describes the theoretical and practical bases for phase sensitive x-ray imaging. Chapter 4 describes the image quality metrics examined in this study. Chapter 5 describes the prototype, the geometry used for the study, the methodology, and the results of the investigation. Finally, Chapter 6 presents a summary of the investigation and its findings, as well as potential future investigations to expand upon this research.

Chapter 2. Background - Conventional X-ray Imaging

Current clinical x-ray imaging methods rely on conventional radiography. This chapter discusses the theoretical and practical background of conventional x-ray imaging.

2.1 X-ray Generation

To generate x-ray beam photons, it is necessary to convert electrons' kinetic energy into radiation by directing an electron beam from the generator's cathode into its anode. Targets used in x-ray applications can typically be tungsten (W) or molybdenum (Mo) [22]. As the electrons interact with the atoms within the target, they lose kinetic energy. This energy loss takes the form of the emission of x-ray photons in a process known as bremsstrahlung radiation [10]. Figure 2-1 illustrates the design and operation of an x-ray source. To increase the number of x-ray photons generated per second, one need only increase the tube current of the source. The energy or amplitude of the x-ray waves can be determined by the user-defined source potential.

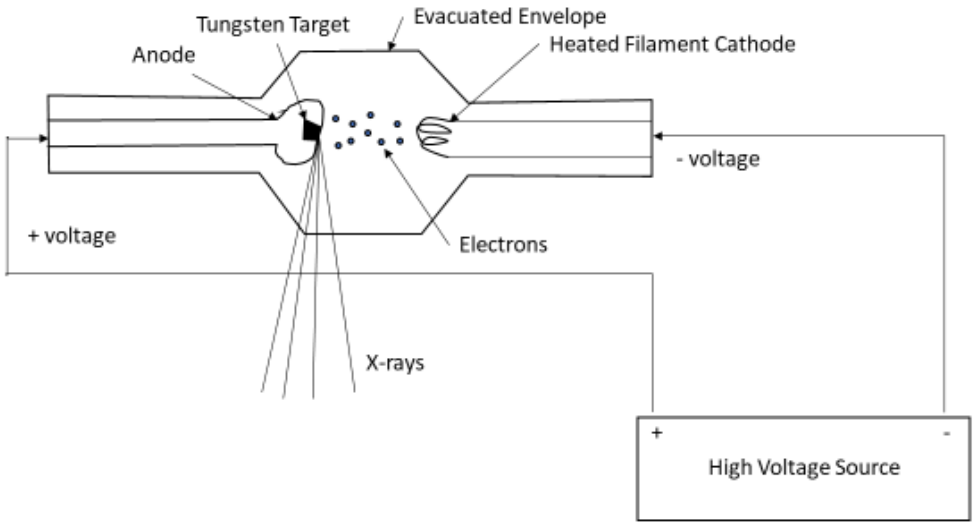

Figure 2 - 1. A design meeting the minimal requirements for the generation of x-rays. It includes a high voltage source attached to an electron source and target (cathode and anode respectively), inside an evacuated envelope.

2.2 X-ray Interactions with Matter

As x-rays travel through a medium other than a vacuum, it is inevitable that they undergo some interaction with the atoms that comprise the medium. The interactions caused by x-rays passing through body tissues impact which detector elements, and at what intensity, the transmitted photons are detected, and thus determine what the image looks like. There are three primary kinds of x-ray-matter interactions: the photoelectric effect, Rayleigh scattering, and Compton scattering [10, 23]. Each phenomenon causes attenuation in x-ray beams, and each has its own attenuation coefficient. Defining the coefficients for the photoelectric effect, Rayleigh scattering, and Compton scatter as μ_{PE}, μ_{RS}, and μ_{CS} respectively, the total attenuation coefficient μ of a material is defined as [24]:

$$\mu = \mu_{PE} + \mu_{RS} + \mu_{CS} \quad (1)$$

The following sections will describe these phenomena.

2.2.1 Photoelectric Effect

The photoelectric effect, causes an x-ray photon to lose all of its energy, which is absorbed by an electron [10]. This phenomenon only occurs when the photon's energy exceeds an electron's binding energy. The excited electron is ejected from, and thus ionizes, the atom [10]. The relationship between the kinetic energy, E_p, of this ejected photoelectron and those of the incident photon, E_o, and the photoelectron's binding energy, E_b, is defined as:

$$E_p = E_o - E_b \tag{2}$$

An electron cascade then occurs, whereby an electron from the adjacent, lower energy ring will fill the hole left by the emitted electron [10]. The process repeats until the lowest energy band loses an electron to the next highest ring [10]. The electrons' transitions from band to band cause the release of either characteristic x-rays (λ_i) or auger electrons [10]. This phenomenon is most likely to occur when the incident photon's energy is just above or equal to the electron's binding energy in its shell (also known as the k edge), and when the electron is tightly bound (as it is in the K shell) [10].

The photoelectric effect is not the most common x-ray-matter interaction to occur in soft tissue, with the probability of absorption being proportional to $\frac{Z^3}{E_o^3}$, where Z is the atomic number of the material encountered [10]. However, the phenomenon still plays a role in image formation. In fact, many x-ray detectors rely on photoelectric absorption as the primary interaction between the detective elements and the incident photons [10]. Contrast agents used in conventional radiography also rely on the phenomenon. Figure 2-2 illustrates the process of the photoelectric effect.

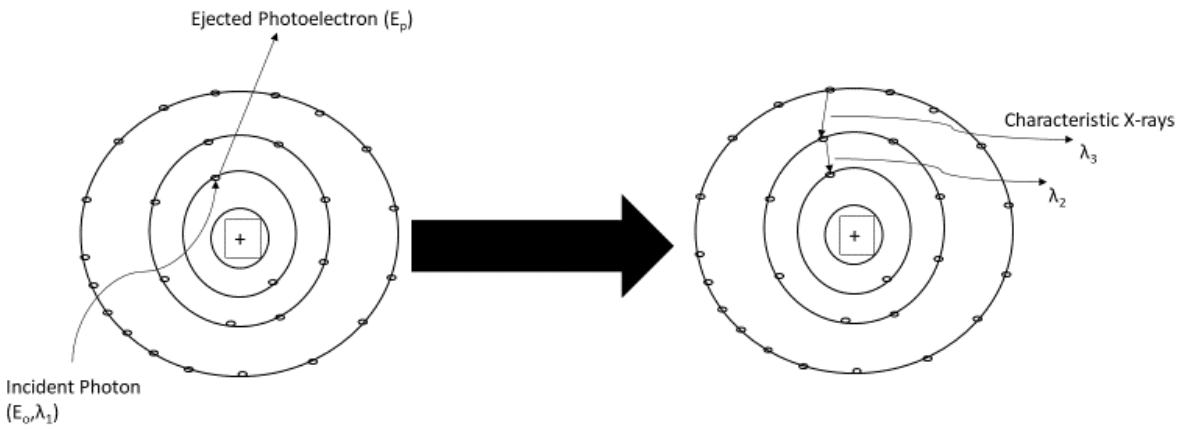

Figure 2 - 2. Illustration of the photoelectric effect.

2.2.2 Rayleigh Scattering

While the photoelectric effect occurs when a single electron is excited, Rayleigh scattering occurs when an entire atom is excited by an incident photon [23]. The absorbed energy causes phase oscillations in the atom's electrons [10]. This causes the electron cloud to emit a photon, whose energy is equivalent to that of its incident counterpart, albeit its trajectory is changed slightly. Rayleigh scattering is most common in low energy imaging, such as conventional mammography (between 15 and 30keV), but not so much in typical diagnostic x-ray imaging (between 20 and 80keV) [10]. Figure 2-3 illustrates the Rayleigh scattering process.

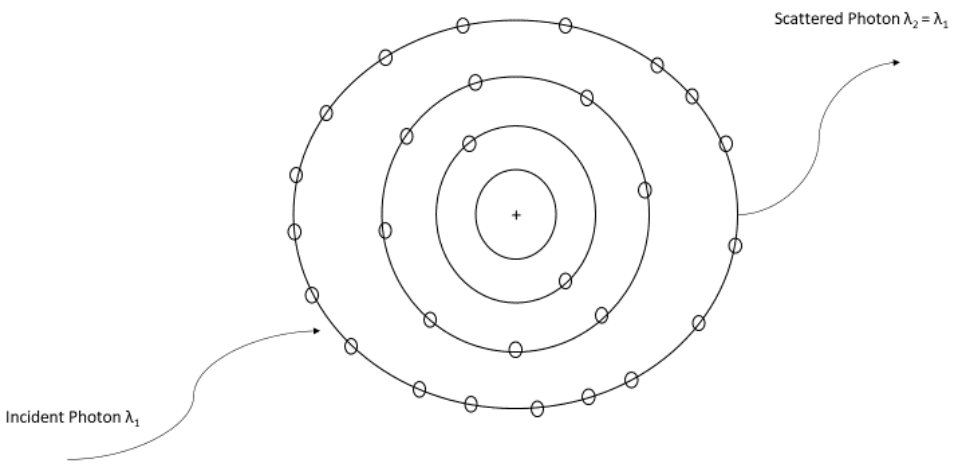

Figure 2 - 3. Illustration of Rayleigh scattering. Note the slightly altered trajectory of the scatter photon from that of the incident photon.

2.2.3 Compton Scattering

Compton scattering is the most common attenuating event to occur in diagnostic x-ray imaging of soft tissue [10]. Usually, the phenomenon occurs when an incident photon and a valence electron interact. Valence electrons have very low binding energies, hence the frequency with which Compton scattering occurs. The interaction causes only some of the incident photon's kinetic energy to transfer to the impacted electron. The electron thus ejects from the atom, while the photon is scattered, moving with less kinetic energy on an altered trajectory. The energy of the incident photon's relationship with the ejected electron, E_{e^-}, and the scattered photon, E_p, is defined as [10]:

$$E_o = E_{e^-} + E_p \tag{3}$$

Since the valence electron's binding energy is so low, it can be safely ignored. The scattered photon may experience interaction with yet another atom via the photoelectric effect, Rayleigh scattering, Compton scattering again, or not at all as it continues through tissue. In

relation to the incident photon's energy and the angle of deflection, θ, the scattered photon's energy can be defined as [10]:

$$E_p = \frac{E_o}{1 + \frac{E_o}{511keV}(1 - \cos(\theta))} \quad (4)$$

There are limits to the amount of energy transferred and the size of the angle of deflection [10]. These limits are due to the laws of conservation of momentum and of energy. The incident photon can transfer up to 511keV to the ejected electron, hence the $\frac{E_o}{511keV}$ term in (4), at a 90° deflection angle, and 255keV at 180° [10]. It can be seen from (4) that higher energy incident photons will yield smaller angles of deflection, and lower energy photons will yield larger angles of deflection. Since conventional diagnostic x-ray imaging employs beams with energies between 20 and 80keV, we can expect relatively high angles of deflection due to Compton scattering. For Compton Scatter to occur, the energy of the incident photons must be much higher than the binding energy of the valence electron. Thus the probability of Compton scatter occurring increases as photon energy increases, unlike the probabilities of Rayleigh scatter and photoelectric absorption [10]. While diagnostic x-rays typically use energies below 100keV, they do meet the energy requirement for Compton scattering. The phenomenon is illustrated in Figure 2-4.

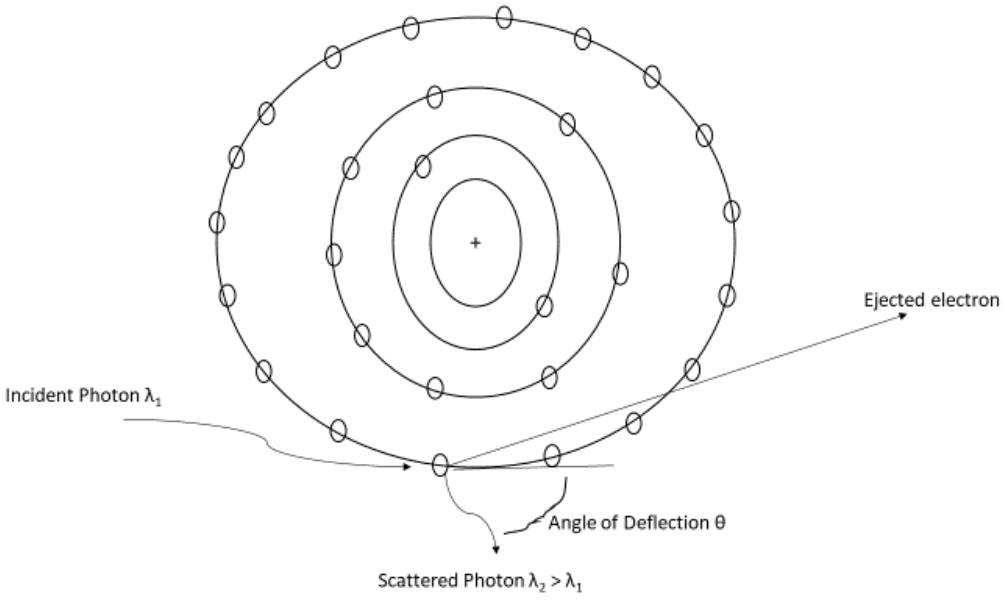

Figure 2 - 4. Illustration of Compton Scattering.

2.3 How Attenuation-causing Phenomena Help Form an Image

The attenuation caused by the three phenomena just described is crucial to conventional diagnostic x-ray imaging. Different beam intensities at each detector element are translated into pixel values. Therefore, if one type of tissue has a larger attenuation coefficient than others, one will be able to distinguish that tissue from its surroundings because it will appear relatively darker. This is due to a decrease in the number of photons passing through the tissue and reaching the detector. If a very thin sample of tissue of thickness x were being imaged, the number of photons lost to attenuation (n), out of a total N_o incident photons, is defined as [10]:

$$n = N_o \mu x \tag{5}$$

Specifically, μ is defined as the linear attenuation coefficient, which conveys the number of photons lost per unit thickness (typically cm) from a monoenergetic beam [10]. As the

material's thickness increases, however, the relationship between the number of lost photons and the object's thickness is not linear [10]. Therefore, the relationship between the number of transmitted (i.e. those that pass through the material) photons, N, and the tissue's thickness can be defined as [10]:

$$N = N_o e^{-x\mu} \tag{6}$$

It is important to recall that, when x-rays pass through a material of a certain thickness, the probability that a photon will interact with an atom is dependent on how many atoms are present per volume of the material [10]. To more accurately model the number of transmitted photons, the linear attenuation coefficient is normalized to the material's unit density in g/cm^3, ρ_o. The result is referred to as the mass attenuation coefficient, and is expressed as $\frac{\mu}{\rho_o}$ cm^2/g [10, 25]. The model for N for a material of density ρ and thickness x then becomes:

$$N = N_o e^{-\left(\frac{\mu}{\rho_o}\right)\rho x} \tag{7}$$

This attenuation model is the bedrock of conventional x-ray diagnostic imaging theory.

Chapter 3. Background - Phase Sensitive X-ray Imaging Theory

Conventional x-ray imaging is entirely based on the attenuation caused by different tissues x-ray beams might pass through. When attempting to distinguish between tissues of very different attenuation coefficients such as soft tissue and bone, or glandular tissue and fat, conventional imaging is perfectly acceptable. As has been stated, however, malignant and benign glandular tissues do not have significantly different attenuation coefficients [16]. This can make conventional x-ray imaging not entirely reliable for detecting potentially malignant neoplasms. If enough x-ray photons were transmitted through the area of concern, then there would be enough contrast between the benign and malign tissues to unambiguously distinguish one from the other. This is due to only slight differences between the attenuation caused by benign tissue and that caused by cancerous tissue. However, such exposure risks surpassing regulatory limits on dosage to the patient. It is therefore necessary to maximize the information received for from the recommended radiation dose. Phase sensitive x-ray imaging is an emerging technology that shows promise in improving detectability for the same dose as conventional x-ray imaging [26]. This chapter will elaborate on the theory behind and techniques used for phase sensitive x-ray imaging, as well as a technique known as phase retrieval.

3.1 Theory and Benefits of Phase Sensitive X-ray Imaging

Wave-particle duality dictates that electromagnetic particles are also waves, and vice versa. This means that all x-ray photons have a sinusoidal waveform and behave as such, while still

existing as a particle. X-ray waves experience all the same phenomena that waves in the visible light spectrum experience. Different media will refract, diffract, and slow down, electromagnetic waves depending on their unique dielectric properties, such as susceptibility [13]. Dielectric susceptibility can be modeled by the refractive index of a material. For x-rays, this index n is complex and can be described as

$$n = 1 - \delta + j\beta \tag{8}$$

where j indicates the imaginary operator ('i' is also used to denote the imaginary component), phase shift is governed by δ, or the refractive index decrement, and absorption is governed by β [13]. The refractive index decrement is approximately 1000 times larger than β, and can be defined as [27]:

$$\delta = \left(\frac{r_e \lambda^2}{2\pi}\right) \sum_k N_k (Z_k + f_k) \tag{9}$$

where r_e denotes the radius of an electron, λ is the x-ray wavelength, and N_k represents the atomic density, Z_k the atomic number, and f_k the real part of the atomic scattering factor for an element 'k'. The phase shift ϕ experienced by x-rays as they pass through biological tissue can be defined as [27]:

$$\phi = -\frac{2\pi}{\lambda} \int \delta(s) ds \tag{10}$$

where the integral is taken over the path of the x-ray, defined as s (δ is constant though as the x-ray continues its propagation along s, it will encounter different tissues, thus $\delta(s)$ is used in equation (9)).

Given how much larger δ is than β, it is easy to see that even minute differences in refractive indices can have a much more significantly impact on contrast than attenuation alone. This makes phase sensitive x-ray imaging a tantalizing prospect for improving detectability compared to conventional procedures using the same dose. There are currently five techniques used in phase sensitive x-ray diagnostic imaging. These include x-ray interferometry, diffraction-enhanced imaging, speckle-based phase contrast imaging, grating-based phase contrast imaging, and in-line phase contrast imaging [16, 28, 29]. All these techniques will be discussed in the following section.

3.2 Phase Sensitive X-ray Imaging Techniques

This section will first discuss x-ray interferometry, then diffraction-enhanced imaging, followed by grating-based phase contrast imaging, speckle-based phase contrast imaging, and will end by discussing in-line phase contrast imaging.

3.2.1 X-ray Interferometry

X-ray interferometry was first developed in 1965 by Bonse and Hart [30]. The design for an interferometric system calls for three perfect crystals in parallel with one another [16]. A synchrotron x-ray beam is directed toward an apparatus of one or more crystals called a monochromator [16]. The monochromator is arranged such that the x-ray beam's incident angle causes only photons of the desired energy to Bragg reflect toward the parallel crystals [16]. Passing through the first crystal causes the beam to split. The second crystal reflects the two beams back toward each other. One of the beams passes through the object being imaged before converging with its counterpart [16]. The object causes the x-rays passing

through it to experience a phase shift. When both beams recombine when passing through the third, analyzer crystal, they will interfere with each other [16]. The fringe pattern generated by the interference will be seen by the detector behind the analyzer. By taking multiple images of the sample from different angles around the sample, one can use the technique for computed tomography (CT), whereby a reconstruction is produced of a map of the samples refractive indices [16]. To yield the best results, it is necessary that the three crystals be aligned nearly perfectly, and that they be crafted from the same crystalline silicon ingot [16]. As the required alignment implies, the technique requires a high degree of precision in its setup. Furthermore, x-ray interferometry is not ideal for imaging that requires higher resolution [16]. Figure 3-1 illustrates the setup for x-ray interferometry.

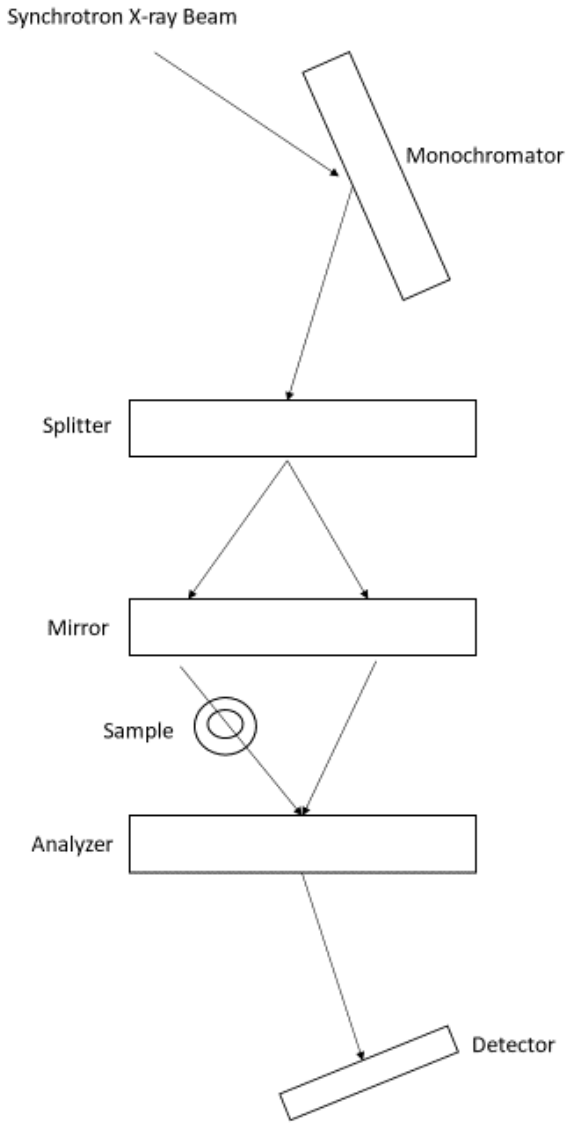

Figure 3 - 1. Illustration of x-ray interferometry. The arrows track the path of the x-rays.

3.2.2 Diffraction-enhanced Imaging

Diffraction-enhanced imaging, like x-ray interferometry, uses a perfect crystal analyzer [31], albeit for a different purpose. A beam is first Bragg reflected off a double crystal monochromator toward the analyzer. Between the monochromator and the analyzer is the sample, which causes small-angle scatter in the beam [32]. The desired information is Bragg diffracted off the analyzer to the detector. X-ray diffraction due to perfect

crystals has a narrow reflection angular width [32]. This narrow width, combined with a reflectivity that is near unity, can either reject or accept small angle scatter, depending on the analyzer's placement, and therefore convey more information in the formed image [32]. This technique improves contrast because any photons scattered at an angle beyond a few μrad will not be diffracted toward the detector, if the analyzer is perfectly aligned with the monochromator [16]. The range of angular orientation for the analyzer relative to the monochromator is called the rocking curve, and ranges between -5 μrad and +5 μrad [16]. Maximum reflectance is achieved by keeping the analyzer perfectly aligned (0 radians) with the monochromator [16]. Altering the analyzer's orientation relative to the monochromator can cause photons with smaller scatter angles to reflect less while those with larger scatter angles reflect more, thus increasing contrast between different tissues [16]. Detuning the analyzer can yield an image to which both absorption and refraction contribute [33]. If images taken with the analyzer oriented on either bound of the rocking curve, are combined, it is possible to yield images due purely to refraction and apparent absorption (including losses to scatter) [16]. While the technique has yielded intriguing results, both in projection radiography and CT [16, 33], it still requires intense, monochromatic beams to ensure an acceptable exposure time. Synchrotron x-ray sources are still the most common used in research, so clinical implementation continues to prove difficult [16, 34]. Figure 3-2 illustrates a basic design for diffraction-enhanced imaging.

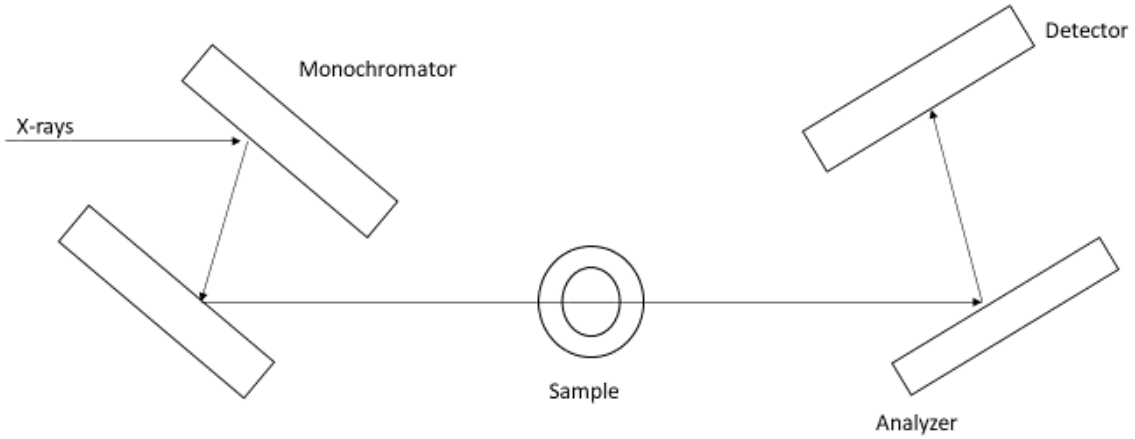

Figure 3 - 2. Illustration of the design for diffraction-enhanced imaging.

3.2.3 Grating-based Phase Contrast Imaging

Grating-based phase contrast imaging, also known as X-ray Talbot interferometry, is a technique that is very similar to x-ray interferometry. Instead of using perfect crystal monochromator and analyzer, however, gratings are placed near the source, behind the sample, and immediately in front of the detector, thus taking advantage of the Talbot effect [28]. The first grating acts as a slit source array, with each source having the requisite spatial coherence for the formation of the image. Previous implementation of the technique used the latter two gratings and a synchrotron source to ensure adequate spatial coherence of the beam [35]. More recent research has indicated that the third grating placed at the source creates enough spatial coherence from each of its slit sources such that a conventional, low-brilliance source can be used instead of a synchrotron [36]. If the period of the source array is the same as that of the analyzer, the phase contrast the beams from each source experience, will interact additively with the others' phase contrasts [28]. The analyzer grating can be manipulated as its silicon

crystal counterpart can to yield different information [28]. The intensity at the detector can be defined as

$$I = I_o \exp\left[-\int_{-\infty}^{\infty} \mu(x,y,z)dy_r\right] * s\left(\frac{x_g}{D} + \theta_r\right) \quad (11)$$

where (x,y,z) represent the coordinates for the sample's reference frame, (x_r,y_r,z) are the coordinates for the x-ray beam's reference frame, D is the distance between the analyzer and phase grating (behind the sample), x_g is the relative displacement between the aforementioned gratings in the direction perpendicular to the beam, θ_r is the refraction angle, and S($\frac{x_g}{D}$) is the shifting curve [28]. The two reference frames are related to each other by

$$\begin{pmatrix} x \\ y \end{pmatrix} = \begin{pmatrix} \cos\phi & -\sin\phi \\ \sin\phi & \cos\phi \end{pmatrix} \begin{pmatrix} \chi_r \\ y_r \end{pmatrix} \quad (12)$$

where ϕ is the rotation angle between x_r and x around the z-axis [28].

As with the previously discussed interferometry technique, grating-based phase contrast imaging can be applied in both projection radiography and in CT, though the former is more clinically feasible than the latter. Furthermore, research is has been done to develop the tomographic technique to reduce exposure time [37]. Figure 3-3 illustrates the design of a grating-based system. The distance between the slits in the gratings determines the spatial resolution of the image [28].

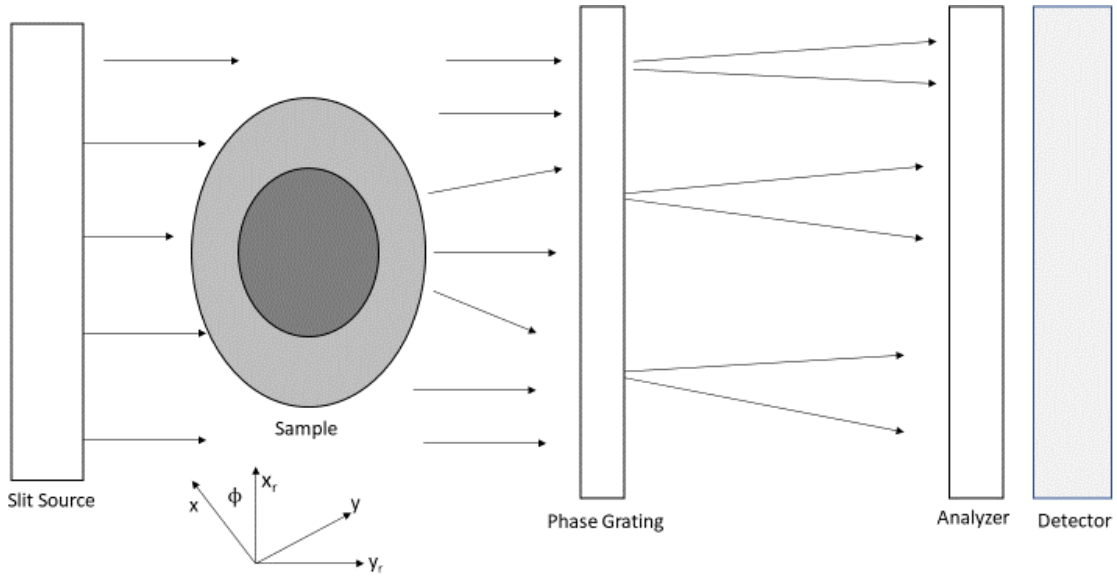

Figure 3 - 3. Illustration of the design for grating-based phase contrast imaging. The axes are denoted below the diagram.

3.2.4 Speckle-based Phase Contrast Imaging

As was implied in the previous subsection, grating-based phase contrast imaging can be time consuming, due to the reduced dose per second. Speckle-based phase contrast imaging does not take as much time as its diffracting agent uses speckles dispersed randomly throughout a chosen material, such as sandpaper [29, 38]. The diffracting speckles act as an analyzer to create the interference pattern before the beam passes through the sample [29]. In this case, the analyzer is simply serving as a diffracting agent to create interference before the beam is incident to the phase object [38]. The x-rays transmitted through the sample are then picked up by the detector which is downstream. If the sample is being monitored over time, an image is first taken of the interference pattern alone, without the sample [39]. With this reference image, the distortion caused by the sample is more easily discerned [39].

Most research in speckle-based phase contrast imaging has used synchrotron sources, but lower coherence, laboratory sources can also be used [29, 39]. While this makes the technique more clinically feasible and less time intensive than others that still rely on synchrotron sources alone, speckle-based phase contrast imaging does have a major drawback: the images yielded are not high resolution [29]. There are methods to improve spatial resolution, but these require multiple images, and thus mitigate the advantage of lower exposure time [29, 40]. Figure 3-4 illustrates the design for a speckle-based phase contrast imaging system.

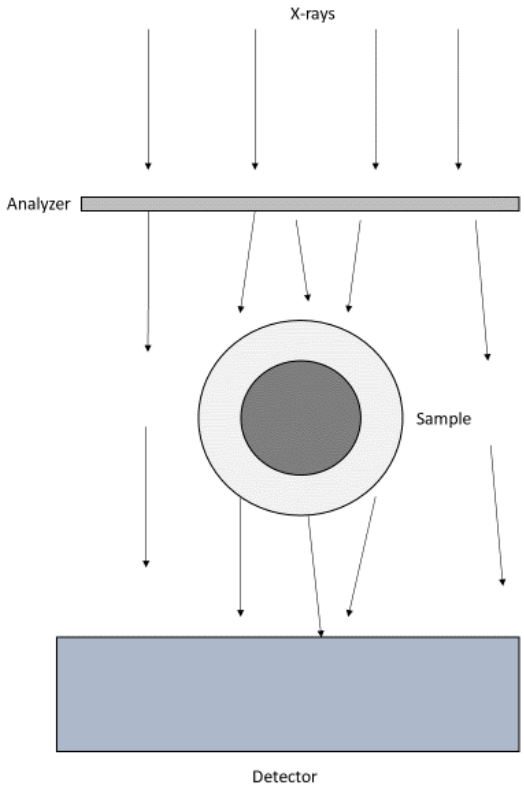

Figure 3 - 4. Illustration of speckle-based phase contrast design.

3.2.5 In-line Phase Contrast Imaging

In-line phase contrast imaging is a common technique used in phase sensitive x-ray imaging, and is the technique used in the research presented in this thesis. It has a relatively simple design, with a source firing a beam through the sample, with the transmitted photons continuing to the detector placed a significant distance downstream [14]. The distance between the sample and the detector has a few effects on the images yielded: magnification of the object, reduction in scatter, and edge enhancement [15-17]. Figure 3-5 illustrates a basic design for in-line phase contrast imaging.

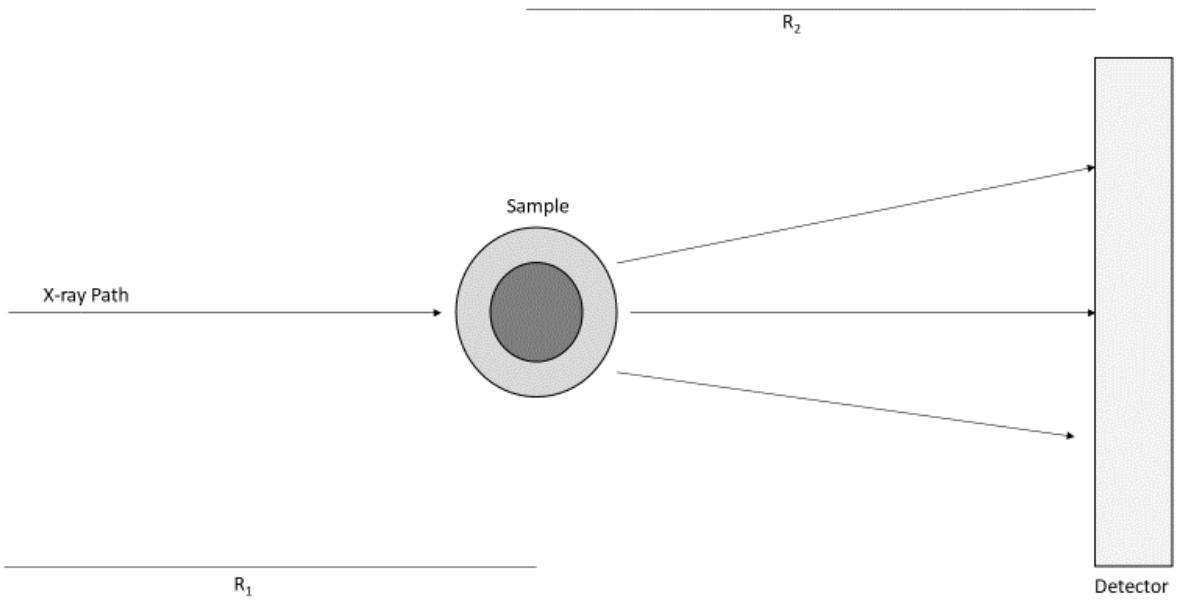

Figure 3 - 5. Illustration of the design for in-line phase contrast systems. R_1 is the SOD, and R_2 is the distance between the object and the detector.

The technique takes advantage of both attenuation and refraction experienced by the x-ray beam as it passes through the object. The distance between the sample and the detector allows for interference patterns due to refraction to become apparent in the

image. These interference patterns allow for better distinguishing between tissues of differing refractive indices. The intensity at the detector for in-line phase contrast imaging can be modelled, under generalized conditions for a polychromatic source, as [15]:

$$I(x,y) = \frac{I_o}{M^2}\left(A_o^2(\frac{x}{M},\frac{y}{M}) - \frac{\lambda R_2}{2\pi M}\nabla^2\left(A_o^2\left(\frac{x}{M},\frac{y}{M}\right)\phi\left(\frac{x}{M},\frac{y}{M}\right)\right)\right) \quad (13)$$

where A^2 is the intensity due to attenuation, ∇^2 is the Laplacian operator, R_2 is the object to detector distance $R_2 = SID - SOD$, and M is the magnification.

The magnification experienced is caused by the distance the x-rays travel to the detector, allowing the attenuation information to be spread out. Thus, there is an improvement in resolving power, while the phase shift becomes more apparent [41]. There are limitations to magnification, as it is possible to produce an image that is too large to be seen entirely by the detector. Magnification is calculated as [41]:

$$M = \frac{SID}{SOD} = \frac{R_1 + R_2}{R_1} \quad (14)$$

It is important to ensure that R_2 does not become so large that the magnification causes focal spot blurring in a phenomenon known as the penumbra effect [23]. The width of the penumbra effect can be defined as $\frac{FS(SID-SOD)}{SOD}$, where FS is the source's focal spot size [23]. Aside from ensuring R_2 is not so large as to render the image too large, other design considerations must be considered for in-line phase contrast imaging. These considerations will be discussed in section 3.2.6.

The edge enhancement seen in in-line phase contrast imaging is due to the difference between phase shifts caused by different tissues within the sample creating fringe effects between the tissues in the image. Thus, the edge between the different tissues is enhanced. This effect can be quantified by the edge-enhancement-to-noise ratio (EE/N) [42]:

$$\frac{EE}{N} = \frac{(Max - Min)}{\sqrt{\frac{\sigma_L^2 + \sigma_R^2}{2}}} \tag{15}$$

where Max denotes the edge's maximum intensity, Min represents the edge's minimum intensity, σ_L^2 is the standard deviation of the background on the left side of the edge, and σ_R^2 is the standard deviation of the background on the right side of the edge [42, 43].

The scatter reduction seen in in-line phase contrast imaging is due to the air gap introduced by R_2. This incidental property helps improve contrast in the image [44]. Contrast can also be improved by introducing a contrast agent to the sample, if possible. Instead of improving the attenuation contrast as is usually done in conventional imaging, microbubbles can be used as a phase contrast agent. The feasibility of the technique has been established in prior research [42, 45, 46]. The microbubbles act in a similar fashion to analyzers used in previously discussed phase sensitive imaging techniques. The bubbles consist of a gas infill within a shell made from various organic materials and can be injected into a phantom for research, or even a live subject for progression and treatment monitoring [42].

3.2.6 Other Design Considerations for In-line Phase Contrast Imaging

As was stated for interferometric techniques, a monochromatic, coherent source is required, hence the use of monochromators, gratings, synchrotron sources, or some combination of the three features in their design [47, 48]. These design requirements are necessary because there exists no truly coherent x-ray source, but rather noncoherent or only partially coherent sources [15]. One advantage of in-line phase contrast image is that a monochromatic source is not a strict requirement. From equation (13), the $\frac{\lambda R_2}{M}\nabla^2 A_0^2\phi$ term does not oscillate [15]. Therefore, the different energy x-ray beams from a polychromatic source cannot destructively interfere with one another [15]. This means that temporal coherence of the x-ray beam is not crucial to in-line phase contrast imaging [15, 44]. However, the spatial coherence is very important to the technique. The coherence width is the farthest distance two points can be apart while interference effects can still be observed [49]. It can be modelled as:

$$L_{transverse} = \frac{2\lambda R_1}{s} \tag{16}$$

where s is the focal spot size of the monochromatic source [15]. Since a photon's wavelength is defined as

$$\lambda = \frac{hc}{E} \tag{17}$$

where h is Planck's constant, c is the speed of light, and E is the energy of the photon in joules. For diagnostic x-ray imaging, the wavelength will be very short, and thus R_1, or the SOD, would need to be quite large before the monochromatic coherent length

would be clinically feasible. Fortunately, the transverse coherent width ($L_{transverse}$) is only part of the picture for the coherence requirement for phase contrast imaging. The diffraction of the x-rays due to their passing through the sample is the other component. The phase-space shearing length L_{shear} can be calculated as

$$L_{shear} = \frac{\lambda R_2 |\vec{u}|}{M} \tag{18}$$

where $\vec{u}$ denotes the object structural component of spatial frequency [50]. The ratio of L_{shear} to $L_{transverse}$ is then used to determine the coherence effects on the phase contrast visibility of the object structure component. The ratio is expressed as [50]:

$$\frac{L_{shear}}{L_{transverse}} = \frac{sR_2|\vec{u}|}{MR_1} = \frac{s(M-1)|\vec{u}|}{M} \tag{19}$$

The ratio is independent of wavelength. So, given an object structure component of frequency, the wave-field will be coherent over the shearing length if $\frac{L_{shear}}{L_{transverse}} \ll 1$, and incoherent if $\frac{L_{shear}}{L_{transverse}} \geq 1$ [50]. Since focal spot size is typically on the scale of µm, and $R_2 < MR_1$, the former condition will typically be met. Microfocus x-ray sources used with large SODs can yield larger transverse coherent widths [15, 19].

Another design consideration that needs to be accounted for is the fact that polychromatic sources generate x-rays of energies lower than the setting specified by the technician or researcher. Some of the x-rays, called “soft” x-rays, are so low energy that none of them will transmit through the sample, and instead either be absorbed, and thus not contribute to the image [10]. Any live patient would therefore risks being

exposed to much more ionizing radiation than is necessary for the procedure. Therefore, it is common practice to implement a technique known as beam hardening to filter those lowest energy photons from the beam before it is incident to the subject. A typical implementation for this filter is to simply place a sheet of attenuating material immediately in front of the source, such as a thin sheet of aluminum. The thickness of the filter can be adjusted as necessity dictates.

3.3 Phase Retrieval and Phase-attenuation Duality

As has been previously stated, in-line phase contrast results in an image with both attenuation and phase contributions to the image. While the efficiency of the dose used is improved compared to that of conventional radiography, it is necessary to perform phase retrieval on the image, once it has been corrected for noise and scatter, to fully benefit from the technique. It entails the retrieval of the phase map $\phi(r)$ from the attenuation and phase image, and relies on the complementary nature of the two contributions [12]. One of the retrieval methods that uses the complementary relationship is based on the principle of phase-attenuation duality (PAD).

Recall that the phase shifts the x-rays undergo while passing through tissue are dependent on the electron density ρ. Wu et al. determined that the electron density could be modelled as [12]:

$$\rho_{e,p}(r) = -\frac{1}{\sigma_{KN}} \log_e \left(\hat{F}^{-1} \left(\left(\frac{\hat{F}\left(M^2 I(Mr; R_1 + R_2)\right)}{I_{in}\left(1 + 2\pi\left(\frac{\lambda^2 r_e R_2}{(M\sigma_{KN})\boldsymbol{u}^2}\right)\right)} \right) \right) \right) \tag{20}$$

where $I(r;R_1+R_2)$ represents the image intensity at the detector, I_{in} is the intensity at the entrance, $\hat{F}$ is the two-dimensional Fourier transform operator, $\hat{F}^{-1}$ is its inverse, and **u** is the spatial frequency vector in the object plane [12]. The ratio $\frac{\lambda r_e}{\sigma_{KN}} \gg 1$ indicates the sensitivity of the change in phase [12]. The variable σ_{KN} is the cross section of the Compton scatter of a single free electron, and is derived as

$$\sigma_{KN} = 2\pi r_e^2 \left(\frac{1+\eta}{\eta^2} \left(\frac{2(1+\eta)}{1+2\eta} - \frac{1}{\eta} \log(1+2\eta) \right) + \frac{1}{2\eta} \log(1+2\eta) - \frac{1+3\eta}{(1+2\eta)^2} \right) \quad (21)$$

where $\eta = \frac{E_{photon}}{m_e c^2}$, which is the energy of the photon divided by the resting electron energy [12]. The phase map A(**r**) can be defined as $A(\boldsymbol{r}) = e^{-\frac{\sigma_{KN}}{2}\rho_{e,p}(\boldsymbol{r})}$, where **r** indicates the path of the x-ray [12]. PAD-based phase retrieval has been found to cause little degradation in spatial resolution in the images examined [51].

Historically, Phase retrieval required multiple images to be taken, or with multiple detectors in a single exposure [12, 52-54]. This rendered an implementation of phase retrieval logistically difficult. Fortunately, the technology has developed such that a single projection image is adequate [12, 20]. Algorithms for Phase retrieval have been developed for years, including a formulation based on the transport of intensity equation, as well as iterative algorithms based on the image intensity equation for in-line phase contrast imaging, with the latter approach handling the retrieval more accurately than the former when complex objects are being imaged [53, 55, 56].

When a micro-focus x-ray source is being used for phase sensitive imaging with phase retrieval, exposure times can be overly long, since those sources use relatively low

current. Increasing the source potential, and thus the energy of the beam, can help shorten exposure time [57, 58]. For this reason, as well as the predominance of Compton Scattering in high energy x-ray beams, in-line phase contrast imaging research has primarily focused on high energy single projection radiography and tomosynthesis. The phase retrieval algorithm developed by Wu and Yan [20] has since been under development to enable implementation of the technique for single projection mid-energy in-line phase contrast images. It is therefore necessary to perform objective characterization of the in-line phase contrast prototype without phase retrieval, to understand the system's capabilities. The eventual goal of this research is to find an optimal balance between exposure and image quality.

3.4 The Research Presented in This Thesis

While the research presented in this thesis does not investigate the efficacy of PAD-based phase retrieval (that is the subject of a concurrent study), it characterizes the lab's prototype in-line phase contrast imaging prototype system for imaging with 60keV. Mid-range energies are considered to include 50kV through 80kV, so 60kV was determined to be a logical starting point for investigating the efficacy of in-line phase contrast imaging at mid-energy. The goal of the investigation presented in this thesis is to characterize the system at 60kV before expanding to include studies of the previously described phase retrieval method's efficacy when applied to mid-energy images. As far as we are aware, this is the first time that objective characterization has been performed for an in-line phase contrast imaging prototype.

Chapter 4 Image Quality Metrics

Before Discussing the research presented in this thesis, it is necessary to provide background information on the image quality measurements used and the concepts behind them. This section presents background information on spatial frequency, the MTF, the NPS, the DQE, and flat field correction.

4.1 Spatial Frequency

Since all three of the image quality measurements mentioned above are represented as functions of spatial frequency, it is necessary to clearly communicate what is meant by the term. Spatial frequency is not dissimilar to temporal frequency, which describes how many times something cycles in a certain amount of time (usually described either as cycles/second or Hz). Instead of describing the number of cycles per unit of time, spatial frequency describes the number of cycles per unit of length, usually in cycles/mm or line pairs/mm [10]. Just as smaller wavelengths imply higher temporal frequency, smaller objects have higher spatial frequency while larger objects have lower spatial frequency. A simplified version of the relationship between spatial frequency is modelled as:

$$F = \frac{1}{2\Delta} \tag{22}$$

where F is the spatial frequency and Δ is the size of the object in mm [10, 59]. This model does not account for the object's periodicity, size, and shape, but the simplified version in equation (22) suffices for this thesis.

Image's pixel values are converted to the spatial frequency domain via the two-dimensional Fourier transform. The one-dimensional operation is described below in equation (23) [10]:

$$G(f) = \int_{-\infty}^{\infty} g(x) e^{-i2\pi f x} dx \tag{23}$$

where f is the spatial frequency, x is the position along the x-axis, and g(x) is the function or model being transformed. The two-dimensional Fourier transform is described as

$$G(u,v) = \int_{-\infty}^{\infty} g(x,y) e^{-i2\pi(ux+vy)} dxdy \tag{24}$$

where u and v are the spatial frequency bins corresponding to the x and y-axes respectively.

4.2 Modulation Transfer Function (MTF)

The MTF is a commonly used metric of image quality for both clinical and research settings. It plots an image's resolution as a function of spatial frequency [10]. Multiple systems' MTFs can be compared to one another to identify the system with the preferred resolving power. The MTF is calculated as the normalized Fourier transform of the line spread function (LSF) [60-64]. Traditionally, the LSF has been obtained as the response to an arrow-slit device. Such a device can be difficult to and expensive to produce or obtain. Another method has been developed that uses an edge device that is simpler to produce in-lab [65, 66].

The edge device is used to obtain the oversampled edge spread function (ESF). Oversampling, or presampling, is a technique whereby the ESF is obtained by arranging the two-dimensional matrix values of the image such that all values are arranged in a one-dimensional array. This is done first by arranging the edge device such that the edge is tilted slightly from the x and y directions [62, 67]. This tilt causes a small shift of the sampling position row to row relative to the edge. This shift is defined as:

$$\Delta x = p\tan(\alpha) \tag{25}$$

where p is the pixel pitch and α is the angle between the y-axis and the edge [62]. One can calculate the average number of rows processed before a shift of one pixel occurs as

$$N_{avg} = \frac{p}{\Delta x} = \frac{1}{\tan(\alpha)} \tag{26}$$

Figure 4-1 shows the tilted edge and the pixel shift. The red line represents the edge.

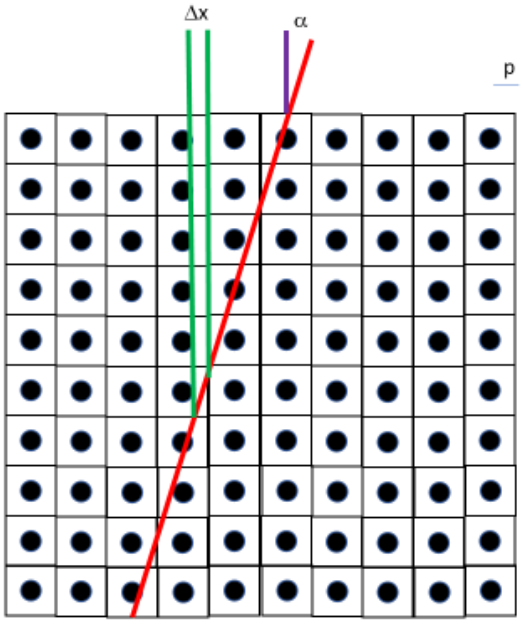

Figure 4 - 1. Illustration of the tilted edge device and the shift effect.

The oversampled ESF is obtained by rearranging the two-dimensional matrix of pixel values into a one-dimensional array. This is done by first choosing N (where N is the nearest integer number to N_{avg}) rows and binning the first pixel of the first row into the first array element [61]. The second array element is filled by the first pixel of the second row. When the first pixel of each row has been binned accordingly, the second pixel of the first row is binned, and so on until the last pixel of the N^{th} row is binned into the last array element [62]. It is assumed that the pixel values have been sampled with a regular subsampling grid, with a sampling distance of $\frac{p}{N}$ regardless of the actual sampling distance due to the shift [62]. This process can be repeated for multiple groups of adjacent N lines, the ESFs of which can be averaged to reduce noise.

As was implied previously, it is not practicable to calculate the oversampled MTF directly from the oversampled ESF. The oversampled LSF still needs to be calculated beforehand. It is calculated by taking the derivative of the oversampled ESF:

$$LSF(x) = \frac{d}{dx} ESF(x) \tag{27}$$

When the LSF has been smoothed by curve fitting, the MTF can be derived by taking the Fourier transform of the LSF:

$$MTF(f) = \int_0^\infty LSF(x) e^{-i2\pi xf} dx \tag{28}$$

The MTF conveys the resolving power as it depends on spatial frequency, and therefore also shows the cutoff spatial frequency of the imaging system. This cutoff frequency is

defined as the spatial frequency at which the system's resolution yields 10 per cent contrast [68]. The imaging system with the highest cutoff frequency is the one with the best resolving power. The MTF is also useful in calculating a system's DQE [69], which will be discussed later in this chapter.

4.3 Noise Power Spectrum (NPS)

The Noise power spectrum is a measurement of the noise texture of an image, or rather the dependence of the noise variance on spatial frequency [10, 70]. It reports the variance for each spatial frequency component found in the noise image [71]. The noise image is found by averaging multiple images together and subtracting the mean image from one of the acquired images. Squaring the absolute value of the noise image's two-dimensional Fourier transform yields the two-dimensional NPS:

$$NPS(u,v) = \left| \iint_0^\infty (I_i(x,y) - I_{mean}) e^{-i2\pi(ux+vy)} dxdy \right|^2 \tag{29}$$

where I_i is one of the images acquired and I_{mean} is the average image, and $(I_i(x,y) - I_{mean})$ is the noise image [64, 70-72]. With the NPS one can see how the system behaves towards its noise input. The variance of the entire noise image can be determined by integrating the NPS over all spatial frequencies [10]:

$$\sigma^2 = \iint (NPS(u,v) du dv) \tag{30}$$

There are two kinds of noise that the NPS can measure: uncorrelated and correlated noise. Uncorrelated noise's autocorrelation function is not trivial, while correlated noise's is trivial. Due to its independence of spatial frequency, the uncorrelated, or "white," noise is typically

reduced in the image or images via correction or filtering. In this study, flat field correction was used to reduce white noise. Figure 4-2 illustrates the appearance of white noise and correlated noise when their noise power spectra are calculated. White noise is much higher in amplitude than correlated noise, so it is essentially impossible to see the correlated noise when the white noise is present.

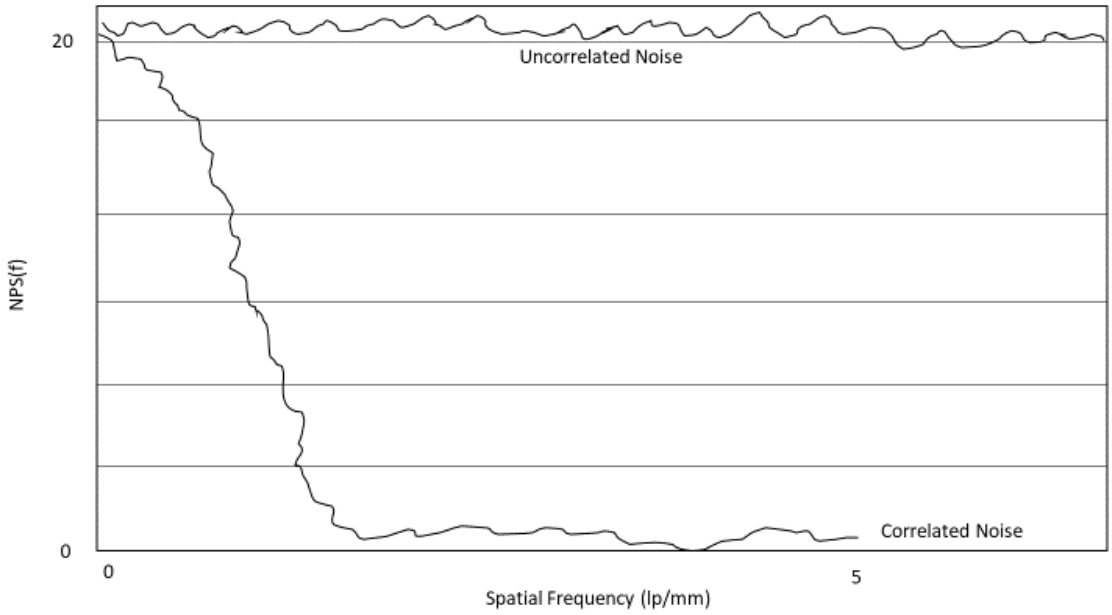

Figure 4 - 2. Illustration of correlated and uncorrelated NPS.

As the NPS measures the noise variance of the input, it is much more useful to imaging scientists than it is to any technician or other clinical professional. It must be considered during the design and testing of imaging systems [10]. This is especially true for computed tomography (CT) systems, since the three-dimensional images require reconstruction from multiple projection data, and there are different algorithms for the process [10]. The NPS is also important for the calculation of an imaging system's DQE, which will be discussed in the following section.

4.4 Detective Quantum Efficiency

The DQE describes the SNR of the system as a function of spatial frequency [10]. Another way to describe it is as the ratio of the output SNR^2 to the input SNR^2 [73]:

$$DQE(f) = \frac{SNR_{output}^2}{SNR_{input}^2} \tag{31}$$

where SNR_{input} is defined as

$$SNR_{input} = \frac{N}{\sigma} = \frac{N}{\sqrt{N}} = \sqrt{N} \tag{32}$$

in which N is the mean photon fluence incident to the system and σ is the noise per pixel [10]. The square of the output SNR is dependent on the MTF and NPS:

$$SNR_{output}^2 = \frac{MTF(f)^2}{NPS(f)} \tag{33}$$

The DQE can thus also be defined as

$$DQE(f) = \frac{s(0)^2 MTF(f)^2}{q * NPS(f)} \tag{34}$$

where $s(0)^2$ is the square of the mean pixel value of the image, and q is the total input quanta per mm^2 to the system [10, 64, 74, 75].

Particularly in polychromatic x-ray imaging, it is possible for some x-ray photons to be so high energy that, while they are incident to the detector, they are not properly absorbed by the detector elements. These photons, and the information they contain, therefore simply pass through the detector without contributing to the generation of the image. The DQE is an important metric because it conveys what fraction of the total

number of photons which are incident to the detector actually contribute to to image formation [75]. Comparing a system's DQE to that of others can help inform an imaging scientist which system or design will ensure maximum image resolution for the given exposure to the patient.

4.5 Pertinence to the Research Presented in This Thesis

The three image quality metrics discussed in this chapter are all important to understanding how an imaging system behaves under specified parameters. They can be used to compare new systems to older ones, current systems to their cohorts, or new techniques to older or previously studied ones. The design and procedural specifications for the research presented in this thesis will be explained in further detail in the following chapters.

Chapter 5 Objective Characterization Study of In-Line Phase Contrast Prototype

This chapter presents the methods by which objects were constructed, images and data were processed, and the results of the experiments and comparison thereof.

5.1 Prototype Description and Experimental Design

This section discusses the design of the in-line phase contrast prototype system used for the research presented in this thesis. The first subsection will discuss the source while the detector will be discussed in the second. The third subsection will discusss the design used for this project. Finally, the fourth subsection will discuss the objects used for the experiments.

5.1.1 X-ray Source

The x-ray source used for this study is a hybrid micro focus source (Model L9181-06, Hamamatsu Photonics, Japan) [76]. The term hybrid refers to the source's capability to emit x-rays in a continuous mode and a pulsed mode. When emitting a continuous stream of x-rays, the source's tube potential can range from 40kV to 130kV and its tube current can range from 10µA to 300µA. In its pulse mode, the source can guarantee tube potentials ranging from 80kV to 130kV with tube currents ranging from 50µA to 300µA [76]. The source uses a tungsten (W) target and a beryllium (Be) output window that is 500µm thick.

The source's focal spot size can vary depending on the output power $P = IV$, where I is the tube current and V is the tube potential or voltage. Possible focal spot sizes range

from 16µm to 50µm [76]. The relationship between output power and focal spot size can be defined by the manufacturer as [76]:

$$FS(\mu m) = 0.999P + 10.27 \quad (35)$$

There is a distance of 13mm between the focal spot and the output window, and the beam angle is 100°. The pulsed mode emits at a frequency of 1.67Hz with a duty cycle of 50% [76]. Thus a single pulse consists of a 300msec on time and a 300msec off time. The square waveform can be altered with a signal generator as the input to the source, with which different pulse durations, lengths, and frequencies can be set. The source communicates via a serial interface, and its dimensions are 167mmx319mmx172mm [76]. Figure 5-1 provides a basic illustration of the source.

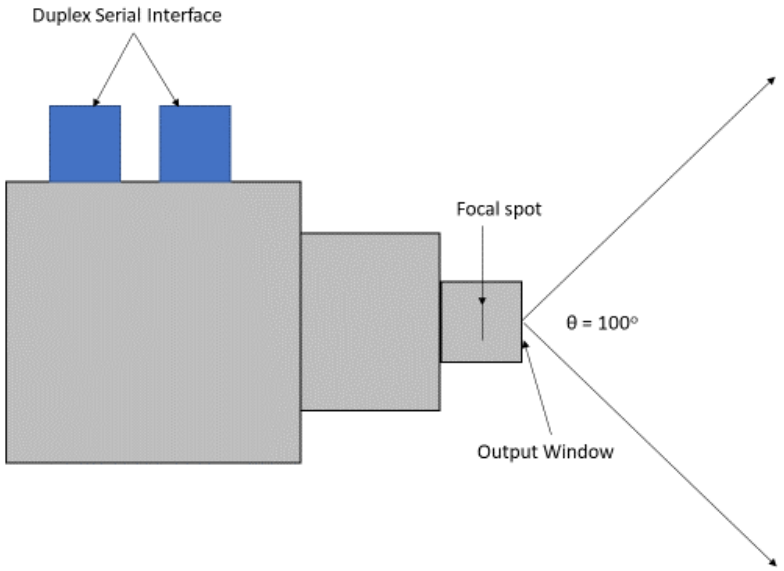

Figure 5 - 1. Illustration of the micro focus x-ray source.

5.1.2 X-ray Detector

A CMOS flat panel detector (Hamamatsu, C7942SK-25) was used for this study. The detector has a pixel pitch of 50µm. It has a photodiode area of 120mmx120mm, and contains 2400x2400

pixels, though the active pixels are only 2316x2316. The scintillator layer (wherein incident x-ray photons are captured and converted to visible light) is made from ceramic type gadolinium oxysulfide (GOS). The top of the detector is covered by 1mm carbon fiber. Figure 5-2 shows a picture of the detector used for this research.

Figure 5 - 2. Photograph of the CMOS flat panel detector

5.1.3 Experimental Design of the In-line Phase Contrast Prototype for This Study

As was previously stated, this thesis presents a characterization study of the in-line phase contrast prototype system when operating with a source tube potential of 60kV and comparing the image quality metrics for that setting to those for 90kV and 120kV

potentials. For all image quality metric experiments the source-to-object distance (SOD) was set to 65.68cm, while the source-to-image distance (SID) was set to 150.876cm. This design yielded a magnification of M = 2.2. The imaged objects, detector, and focal spot were aligned with an optical rail. Figures 5-3 and 5-4 provide an illustration of the design and a photograph of the implemented design respectively.

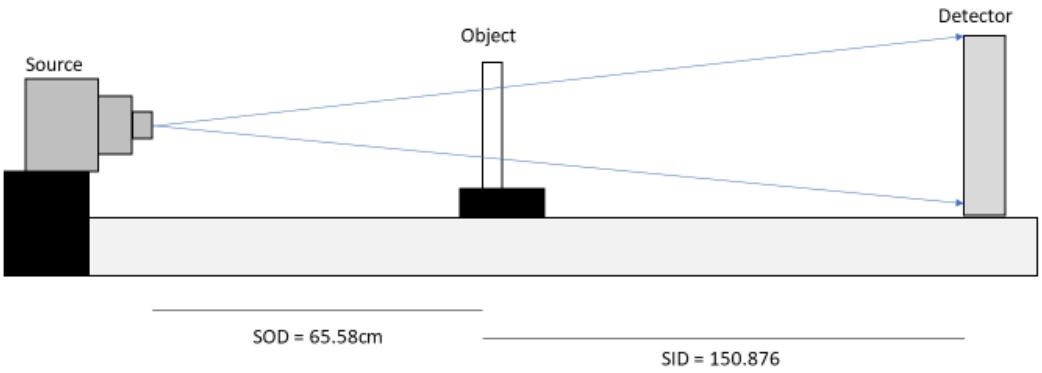

Figure 5 - 3. Illustration of the experimental setup for this study.

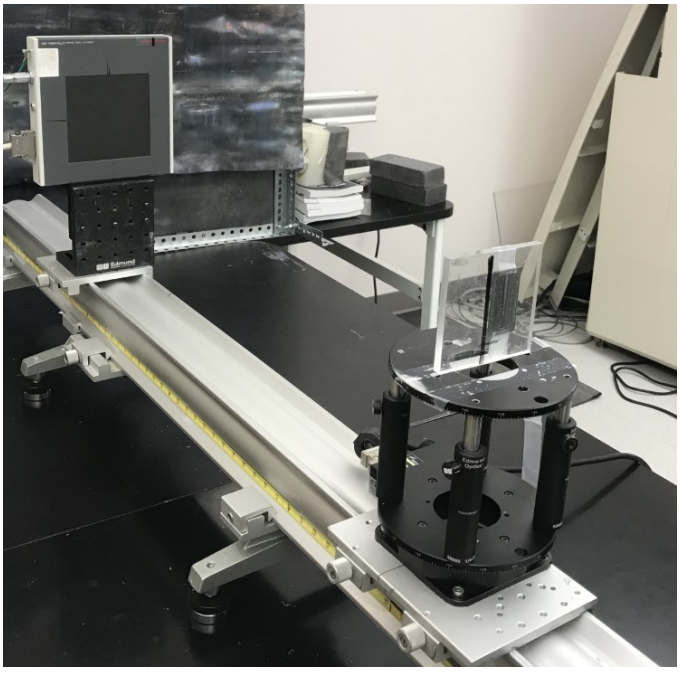

Figure 5 - 4. Photograph of the experimental setup implemented.

Figure 5-4 shows the setup with the angle resolution pattern device, which will be discussed in the next chapter, at the SOD. The other objects used in this study were a tilted edge device and a virtual detector, which were also set at the SOD.

To implement beam hardening, a 1.2mm aluminum (Al) filter was placed immediately in front of the source when emitting a 60kV beam. A 2.5mm Al filter was used for 90kV and 120kV beams. As has been stated, this is done to eliminate any x-rays in the polychromatic beam that are so low energy that they will simply be absorbed by the object, and thus contribute dose without aiding in image formation.

5.2 Objects Used in this Study

5.2.1 Edge Device

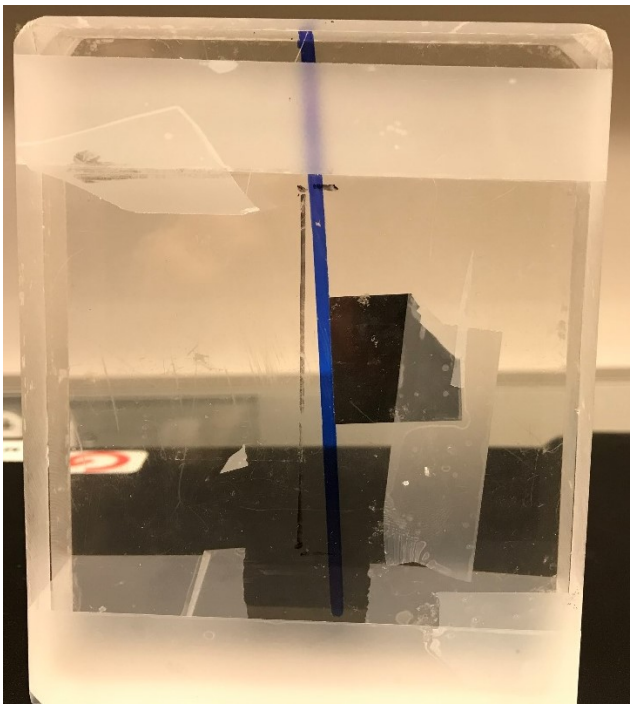

Figure 5 – 5. Photograph of the edge test device

The edge device was assembled by placing a piece of highly attenuating metal between two acrylic slabs. To obtain the oversampled ESF, the metal edge was tilted such that it formed a slight angle with the y-axis. This angle was found to be approximately 3.46°. The edge was made from tungsten (W) and was 50µm thick. The acrylic was cleaned before assembly to remove potentially scattering material from the object. Figure 5-5 provides a photograph of the device. The edge was attached to one slab with scotch tape, and the acrylic slabs were attached the same way. When placing the device, the edge itself was at the SOD, not the front end of the first slab.

5.2.2 Angle Resolution Pattern Device

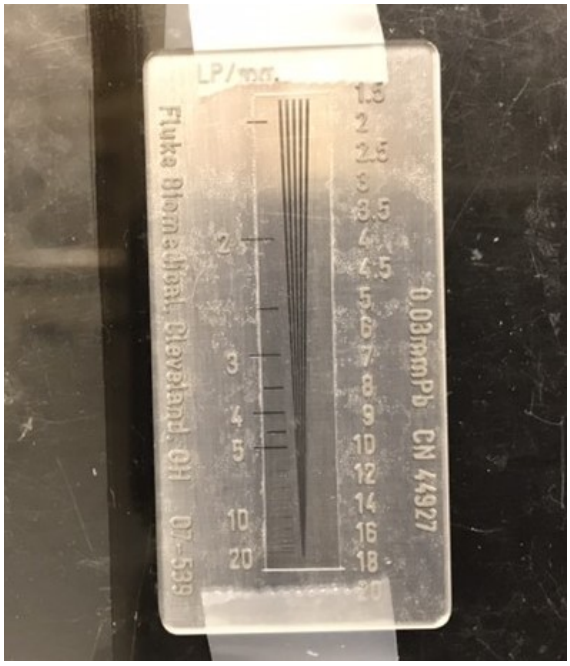

Figure 5 – 6. Photograph of the angle resolution pattern device.

Figure 5-6 provides a photograph of the angle resolution pattern device used for this study. An angle resolution pattern device (Fluke Biomedical, 07-539, Cleveland, Ohio)

was used to confirm the cutoff spatial frequency indicated by the MTFs. An angle resolution pattern is a device crafted from highly attenuating material to test the resolving power of an imaging system. Slits are carved into the material that, in the model used for this experiment, taper toward each other as one's gaze lowers on the device. The decreasing space between the lines corresponds to the increased spatial resolution to clearly distinguish one slit from the other. The angle resolution pattern used in this study was made from a 0.025mm slab of lead (Pb). Subjective and quantitative methods can be employed to evaluate the resolution indicated by images of the angle resolution pattern. It was taped to a single acryclic slab, and was kept as close to parallel with the y-axis as possible, as it is not practical to image the device at a slant. Because this is a quantitative study, the decision was made to focus on the quantitative method, which will be discussed later in this chapter.

5.2.3 Virtual Detector

A virtual detector is used for NPS and DQE evaluation under magnifying conditions [41]. It provides a simple method by which one can account for the apparent size change the imaged object experiences. Most conventional images are taken in what is know as contact mode, for which the imaged object is in contact with the detector, or when SID is insignificantly larger than SOD. While there will undoutbedly be some slight magnification due to the fact that the detector is not in the exact same spot as the object, the effect will be minimal in contact mode. However, the air gap required to ensure coherence in in-line phase contrast imaging ensures that magnification will be significant. Therefore, some mathematical adjustments must be made. These

adjustments include accounting for the apparent change in pixel size between the virtual detector and the real detector and the difference in radiation exposure at the two points. The pixel size at the virtual detector x_m is defined as

$$x_m = \frac{x}{M} \tag{36}$$

where x represents the pixel size of the actual detector [41]. This adjustment impacts the calculation of the NPS. The second adjustment, for radiation exposure, impacts the DQE calculation, and will be discussed in the next section of this chapter. Figure 5-7 illustrates the concept of the virtual detector.

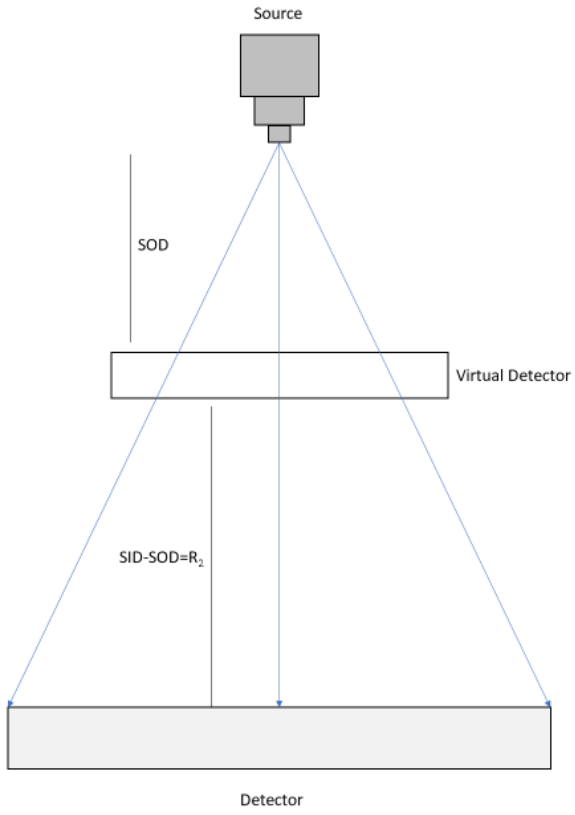

Figure 5 – 7. Illustration of the virtual detector

5.3 Methods

This section presents the methods by which the images and data were acquired and processed. The first subsection will cover the MTF calculation process, while the second will cover the NPS calculation process. The third subsection will cover how data were acquired and processed.

5.3.1 Flat Field Correction

When x-ray images are acquired, it is inevitable that environmental noise and white noise will be present, reducing image quality. When measuring an imaging system's performance, the only form of noise which interests researchers is the noise inherent to the system's interaction with the incident photons. It is therefore necessary to remove as much white and environmental noise as possible from the images. Flat field correction is one image processing method used to remove white noise and was the chosen method for this study. The method uses image subtraction as the noise removal mechanism and requires multiple images to be acquired. First, multiple images are acquired of the object. Multiple "dark" images are then acquired, for which the detector is active, but the x-ray source is not. The final set of images, called "flat field" images, are acquired with both the detector and source active, but with no object between the source and detector. The pixel values seen when acquiring flat field images should be approximately 25% higher than those seen in the object images. The

dark images are meant to capture the environmental noise in the imaging room, while the flat field images capture the white noise inherent to the system.

Once the images are acquired, the image processing is a simple calculation for which the corrected image C can be determined by:

$$C = \frac{m\left(I_{avg} - D\right)}{F - D} \tag{37}$$

where I_{avg} represents the average of the object images, D is the average of the dark images, F is the average of the flat field images, and m is the mean pixel value of the (F-D) term. The quantity of each kind of image taken for each experiment will be specified in their respective subsections.

5.3.2 MTF

This subsection will discuss under what parameters each MTF experimental scenario took place, as well as how the MTF was calculated.

5.3.2.1 Image Acquisition

As was previously stated, the 60kV images were acquired with a 1.2mm Al filter placed in front of the output window, while the 90kV and 120kV images were obtained with a 2.5mm Al filter in the same location. When investigating the MTF, the results reflect only the system's performance, and therefore does not depend on the radiation exposure to the detector. Steps were therefore not taken to keep constant exposure across all three tube potential scenarios. The edge device described in the previous section was placed at the SOD while the detector was placed at the SID.

Three images were acquired of the object, while five were acquired for both dark and flat field images. The object images were obtained with exposure times of 20, 12.5, and 10 seconds at 60kV, 90kV, and 120kV respectively. The dark images were obtained with the same acquisition times as the object images. Flat field images for 60kV, 90kV, and 120kV were acquired with exposure times of 10, 7.69, and 4.76 seconds respectively. The tube current was kept constant at 300µA throughout the MTF experiment, with focal spot sizes of 28.25µm, 37.24µm, and 46.23µm for 60kV, 90kV, and 120kV.

5.3.2.2 Processing and MTF Calculation

The object images were corrected as described in equation (35) before they were analyzed for MTF calculation. The oversampled ESF was then calculated in the manner described in Chapter 4. For each tube potential scenario, the same region of interest (ROI) of 300 rows x 200 columns was cropped from the corrected edge image to calculate the ESF.

Figure 5-8 provides the plot of the unsmoothed, 60kV ESF. The ESF was then convolved with a four-point moving average window to smooth the curve, using the conv MATLAB function.

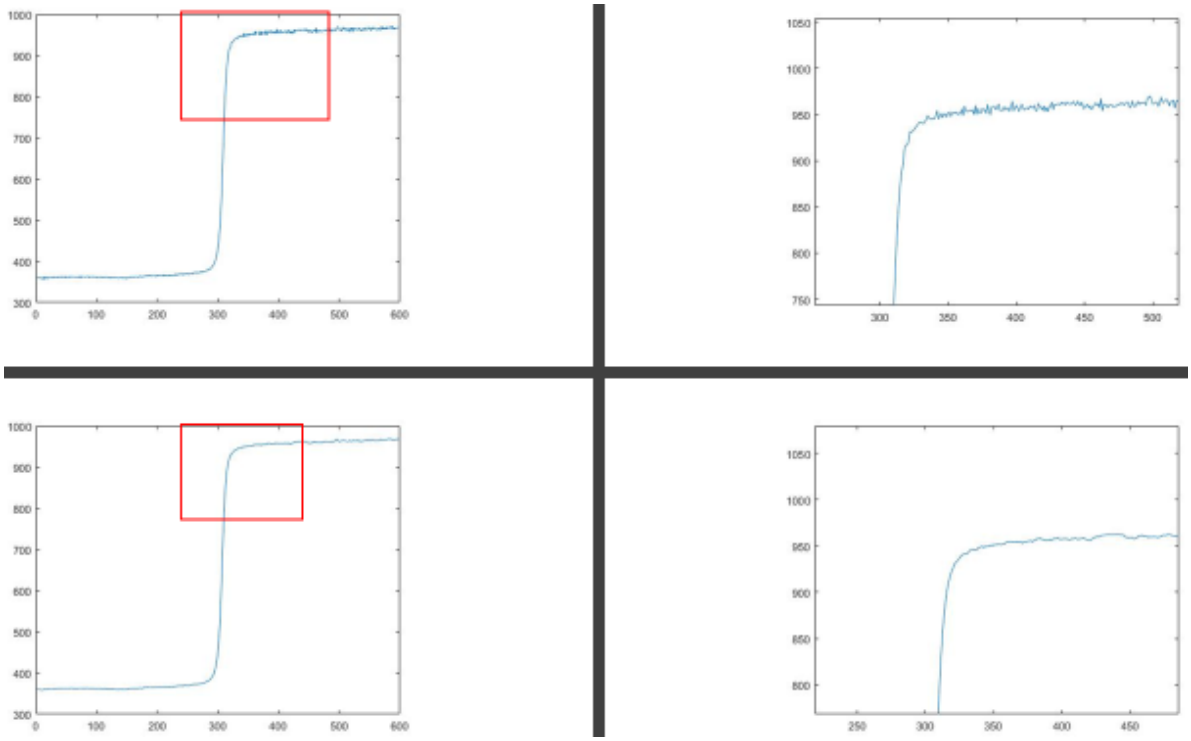

Figure 5 – 8. Plot of the unsmoothed (top row) and smoothed (bottom row), 60kV ESF.

Taking the derivative of the smoothed ESF yielded the LSF. To ensure the MTF would be smooth upon generation, the LSF was curve fitted with a Gaussian function using MATLAB's curve fitting tool. Figure 5-9 provides a plot of the 60kV LSF before it underwent curve fitting through MATLAB's curve fitting toolbox, called by the function cftool. The 120kV LSF was fitted by 2nd order Gaussian functions, while the 60kV and 90kV LSFs were fitted by a 3rd order Gaussian function.

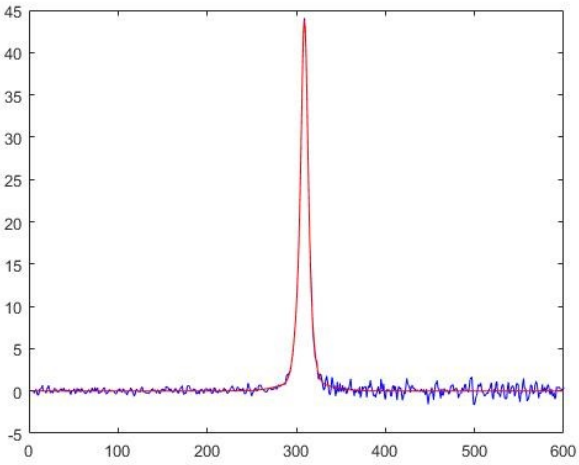

Figure 5 – 9. Plot of the unsmoothed (blue) and curve fitted (red), 60kV LSF.

The fitted LSF then underwent a one-dimensional Fourier transform to calculate the MTF. As the MTF is supposed to be independent of noise, it is expected that it will remain almost the same across all tube potential scenarios. All three MTFs are provided in the next section of this chapter.

5.3.3 Angle Resolution Pattern

This subsection will discuss the parameters under which the images for the angle resolution pattern investigation, as well as how the corrected images were quantitatively analyzed for contrast.

5.3.3.1 Image Acquisition

The angle resolution pattern device was placed at the SOD while the detector remained at the SID. Tube current and potential were the same as they were for the edge device images. The Al filter thicknesses were also kept the same from the edge device acquisitions. For the object and dark images, exposure times were 14.29, 6.67, and 4

seconds for 60kV, 90kV, and 120kV. Flat field images were acquired over exposure times of 14.29, 6.67, and 3.85 seconds for 60kV, 90kV, and 120kV.

5.3.3.2 Processing and Quantitative Analysis

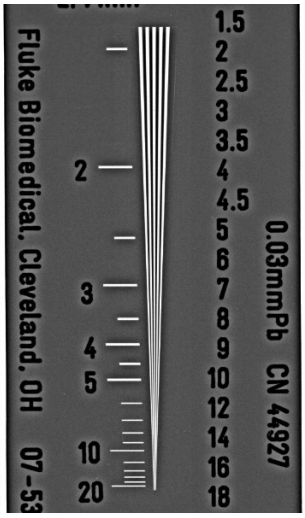

Figure 5 - 10. X-ray image of the angle resolution pattern taken with 60kV.

Figure 5-10 provides the processed image of the angle resolution pattern taken with 60kV. The angle resolution pattern images underwent flat field correction in the same manner as the edge device images did. The corrected images were then loaded into ImageJ, where they were further processed through a filter known as an unsharp mask. The mask used radii of 20, 25, and 30 pixels for 60kV, 90kV, and 120kV respectively.

To quantify the contrast the contrast in the images, the Michelson contrast was calculated. The Michelson contrast C_M can be defined as:

$$C_M = \frac{Max - Min}{Max + Min} \tag{38}$$

where Max denotes the maximum pixel value and Min denotes the minimum pixel value of the ROI. A rectangular ROI is drawn across the slits at the desired location along the spatial frequency axis, and the profile of the pixel values is plotted across the x-axis.

To mitigate the impact of any outliers, two different peaks, representing two different lines, were used to calculate Michelson contrast. The results were averaged together. The threshold for adequate contrast is the same as that of the MTF: 10%, or 0.10. The two peaks with the highest pixel values were chosen for these calculations. Results from this study are presented in the next section of this chapter.

5.3.4 NPS

This subsection details the parameters under which images were acquired for NPS analysis, as well as the method by which they were processed and analyzed.

5.3.4.1 Image Acquisition

When performing NPS analysis that compares images taken with different energies, it is important to maintain constant exposure for all scenarios. This condition applies to the object images, but not to the flat field images. The object images were obtained with tube currents of 287µA, 294µA, and 300µA for 60kV, 90kV, and 120kV respectively. These tube settings yielded focal spot sizes of 27.47µm, 36.70µm, and 46.23µm for 60kV, 90kV, and 120kV. The exposures at the virtual detector at SOD were 10.086mR, 10.114mR, and 10.086mR for 60kV, 90kV, and 120kV. Ten object images and five dark were obtained with exposure times of 7.69, 6.67, and 4 seconds for 60kV, 90kV, and

120kV respectively. Five flat field images were obtained with exposure times of 10, 8.33, and 5 seconds for 60kV, 90kV, and 120kV respectively.

5.3.4.2 Analysis

A slight change was made to the flat field correction process for NPS analysis. Instead of correcting an averaged image, all 10 of the object images were corrected. This is due to the condition seen in equation (29), where a mean corrected image is subtracted from one of the 10 object images. An average image was calculated from the 10 corrected object images. Since variation should be minimal between object images, the choice of which object image to subtract the mean image from is arbitrary. For this study, the fifth object image was chosen. Subtracting the mean image from the object image yielded a noise image, as shown in Figure 5-11.

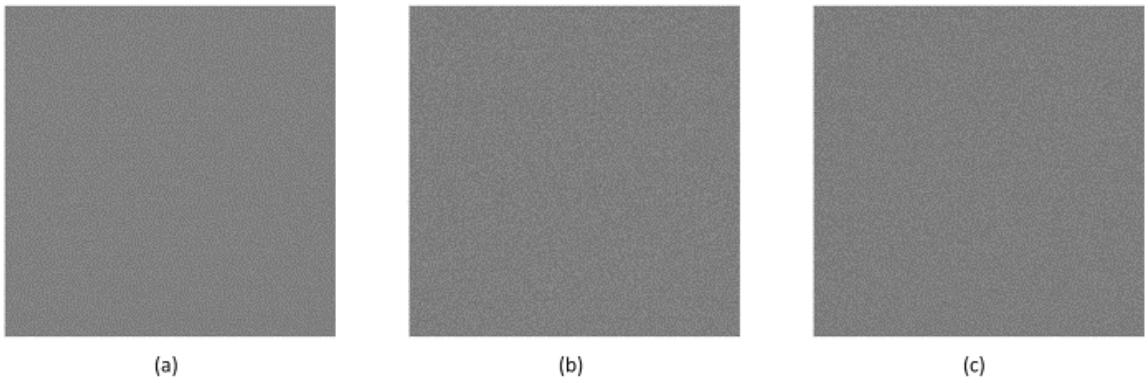

Figure 5 – 11. Noise images for (a) 60kV, (b) 90kV, and (c) 120kV.

The mean pixel value of the average corrected image is then calculated, to be used for DQE analysis. Each noise image underwent zero-mean detrending. From each noise image shown in Figure 6-8, four ROIs were chosen, with one in each quadrant. The ROIs

were 256 pixels x 256 pixels and covered the same areas across all tube potential scenarios. The two-dimensional Fourier transform of each ROI was calculated, and the resulting NPS was calculated as:

$$NPS(u,v) = \left| \iint_0^\infty (I_5 - I_{mean}) e^{-i2\pi(ux+vy)} dxdy \right|^2 * \frac{x_m}{N_x N_y} \quad (39)$$

where x_m is the adjusted pixel pitch from equation (37), and N_x and N_y are the number of rows and columns in the ROI respectively. The $\frac{x_m}{N_x N_y}$ term in equation (39) accounts for the magnification due to R_2. Figure 6-9 provides examples of the two-dimensional NPS for each tube potential scenario and uses heat maps to more clearly label the presence of noise at each spatial frequency. When viewing the two-dimensional NPS, it is important to note that the origin, or center, of the image represents the noise variance at 0 spatial frequency. The spatial frequency then increases as the radius around the origin increases. Figure 5-12 provides intensity maps the two-dimensional NPS for each tube potential scenario.

Figure 5 – 12. Intensity maps of two-dimensional NPS (a) 60kV, (b) 90kV, and (c) 120kV.

Because the NPS is a measurement of noise variance, it is expected that the plots of the data will reflect what is seen in Figure 5-12. The two-dimensional NPS for each ROI is then averaged radially to plot the NPS as a function of spatial frequency. The four NPS calculated for each potential scenario are then averaged, to minimize the impact of any outliers and thus improve accuracy. The resulting NPS plots will be presented in the next section of this chapter. Figure 5-13 provides a visualization of the radial averaging process.

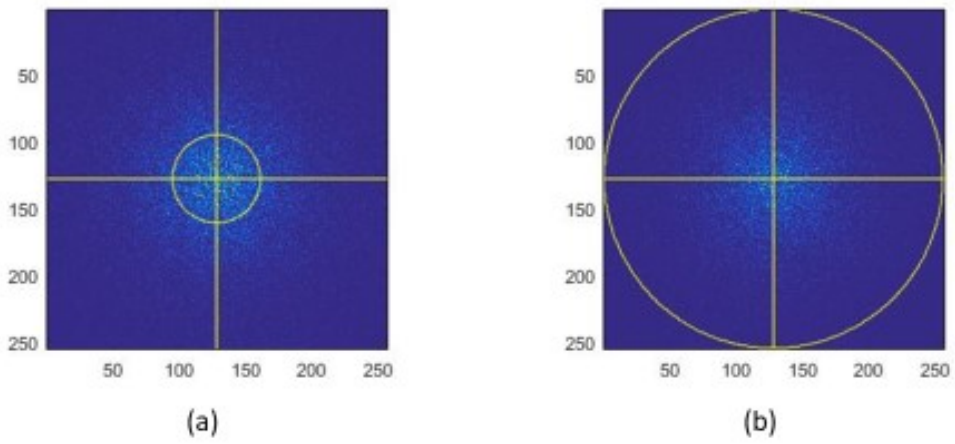

Figure 5 – 13. Visualization of radial averaging of NPS: (a) in progress, (b) complete.

5.3.5 DQE

After the MTF and NPS are calculated, the DQE can then be assessed for each scenario. One further step needs to be taken, however, before the NPS and MTF can be incorporated into the calculation. Recalling that the DQE requires the pointwise square of the MTF to be divided pointwise by the NPS, it becomes necessary to ensure that the NPS and MTF array elements are associated with the exact same spatial frequency. The methods by which the two metrics were calculated did not ensure this on their own, so

it was necessary to interpolate the MTF values at the spatial frequencies used in the NPS calculation. This was done using the interp1 command in MATLAB.

The remaining variables used in the calculation of the DQE are the input quanta, or how many photons are expected to be incident to the detector, and the large area signal, or the mean pixel value of the averaged, corrected image. Table 5-1 provides the values for the input quanta and large area signals for each of the scenarios.

Tube Potential (kV)	Input Quanta (photons)	Large Area Signal
60	990240	1246.2
90	1647700	2199.2
120	1812500	2561.2

Table 5 - 1. Input quanta and large area signals

In addition to the input quanta and the large area signal, another factor must be considered: the magnification. Because the input quanta are based on the SOD, or where the virtual detector is, the DQE must be adjusted, with equation (34) becoming [77, 78]:

$$DQE(f) = \frac{s(0)^2 MTF(f)^2}{q * NPS(f) * M^2} \tag{40}$$

Before proper comparison was done, the DQEs underwent curve fitting with the MATLAB curve fitting tool. The 60kV and 90kV DQEs were fit to a first-degree Gaussian function, while the 120kV DQE was fitted to a second-degree Gaussian. The DQE data are presented and compared in the next section of this chapter.

5.4 Results

This section presents the results of the study. The MTFs are presented first, followed by the results of the angle resolution pattern investigation. The NPS are then presented, followed by the DQEs.

5.4.1 MTF Results

The MTF results indicated that the prototype's cutoff spatial frequency was approximately 14 lp/mm. Furthermore, all three MTFs behaved as expected, in that they were nearly identical when plotted against each other for comparison. Table 5-2 provides the specific cutoff frequencies to each tube potential.

Tube Potential (kV)	60	90	120
Cutoff Frequency (lp/mm)	14.33	14.33	14.109

Table 5 - 2. Cutoff frequencies as determined by the MTF.

Figure 5-14 provides the three MTFs plotted alongside one another, providing visual corroboration of the data in Table 5-2.

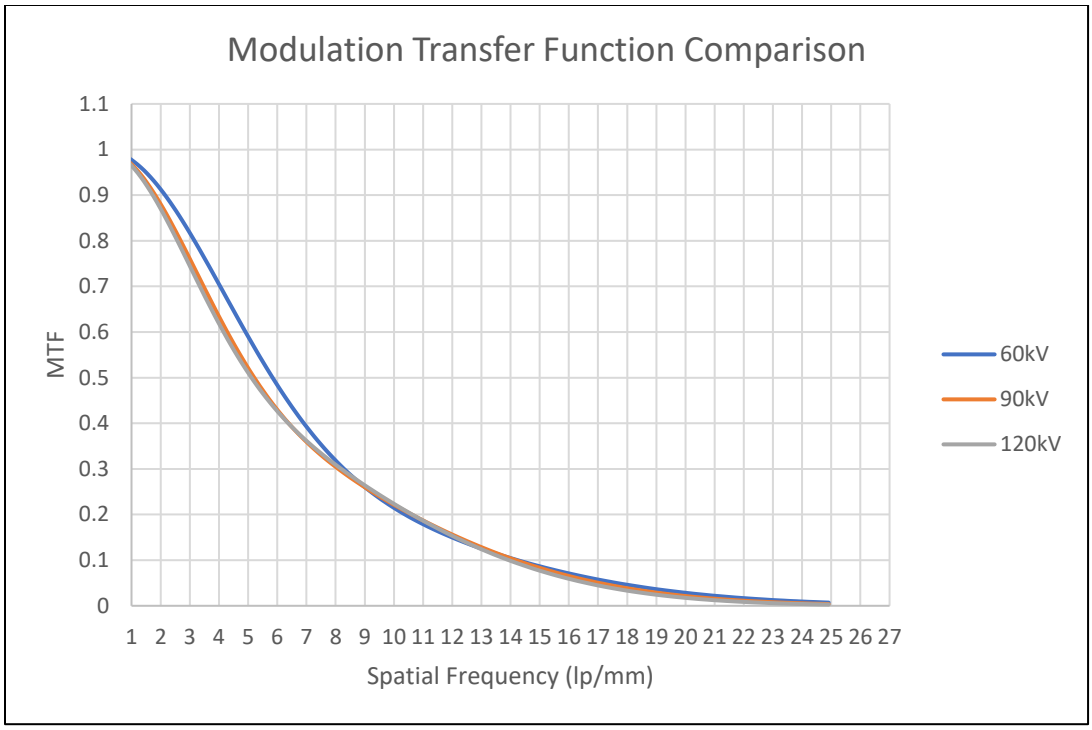

Figure 5 – 14. Plot of the three MTFs in comparison to one another.

As was previously stated, the MTF should not vary significantly as parameters such as tube potential and current change, as it is an indicator of the imaging system's resolving power, and not of the noise variance or input quanta. Therefore, these results match expectations. Further study of the system's cutoff frequency was conducted with the angle resolution pattern investigation, the results of which will be discussed in the next subsection.

5.4.2 Angle Resolution Pattern Contrast

The angle resolution pattern investigation was conducted to confirm the findings in the MTF study. Specifically, it was intended to calculate the contrast at the MTF-indicated cutoff frequency via another method, thus corroborating results. Equation (38) was used to measure the Michelson contrast at the 14 lp/mm mark of the angle resolution

pattern. As with the MTF, the threshold for guaranteed resolvability by the human eye was set to 0.1 contrast. Figures 5-15 shows An ROI chosen from a angle resolution pattern image at 14 lp/mm. Figure 5-16 displays the profile peaks mentioned in the previous section, which were used to calculate the Michelson contrast. Table 5-3 presents the calculated Michelson contrasts.

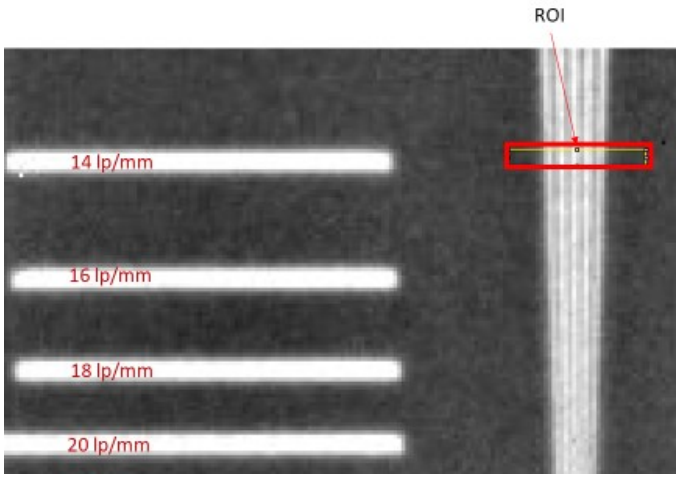

Figure 5 – 15. Image of the ROI used for calculating Michelson contrast (60kV).

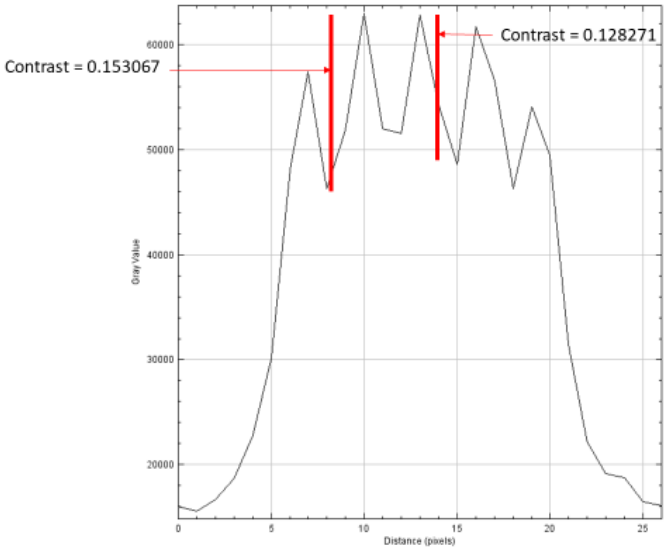

Figure 5 – 16. Example of plotted profile for Michelson contrast calculation (60kV).

Tube Potential (kV)	60	90	120
Michelson Contrast at 14 lp/mm	0.140669	0.109376	0.091063

Table 5 - 3. Michelson contrast results.

While the results in Table 5-3 for 90kV and 120kV seem to contradict those given by the MTF, they do not differ significantly. It is important to remember that the format in which the images were viewed can impact how the image is displayed. Furthermore, these calculations are not entirely exact, but are rather a decent approximation. What is certain is that the cutoff frequency, while not exactly 14 lp/mm, is very close to that resolving power. Thus, the results of the MTF investigation are confirmed.

5.4.3 NPS

The results of the NPS will first be presented separately and then together, for comparison. It is common to see strange behavior around zero frequency in the NPS, this is due to DC effects inherent to the imaging system. Figures 5-17 through 5-19 provide the plots of the NPS for 60kV, 90kV, and 120kV.

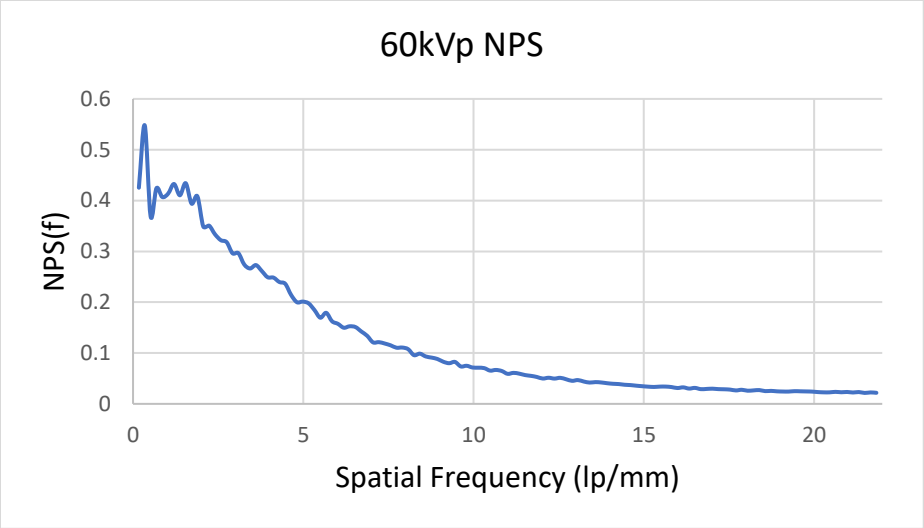

Figure 5 – 17. NPS at 60kV.

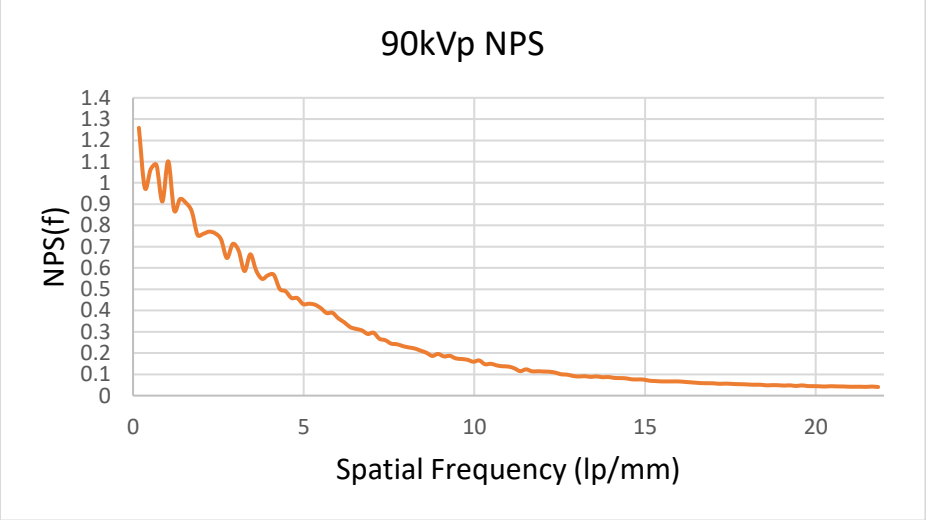

Figure 5 – 18. NPS at 90kV.

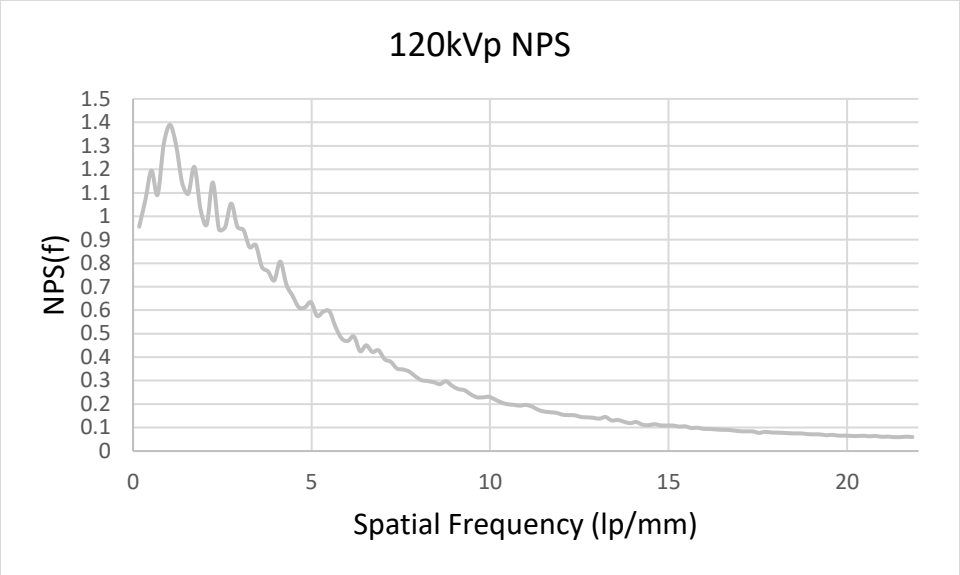

Figure 5 – 19. NPS at 120kV.

While the noise variance decreases as spatial frequency increases, it can be seen from the above figures that the 90kV and 120kV NPS approach zero much more slowly than that for 60kV. Figure 5-20 plots the three NPS together, to compare the trends as well as the DC effects near zero frequency.

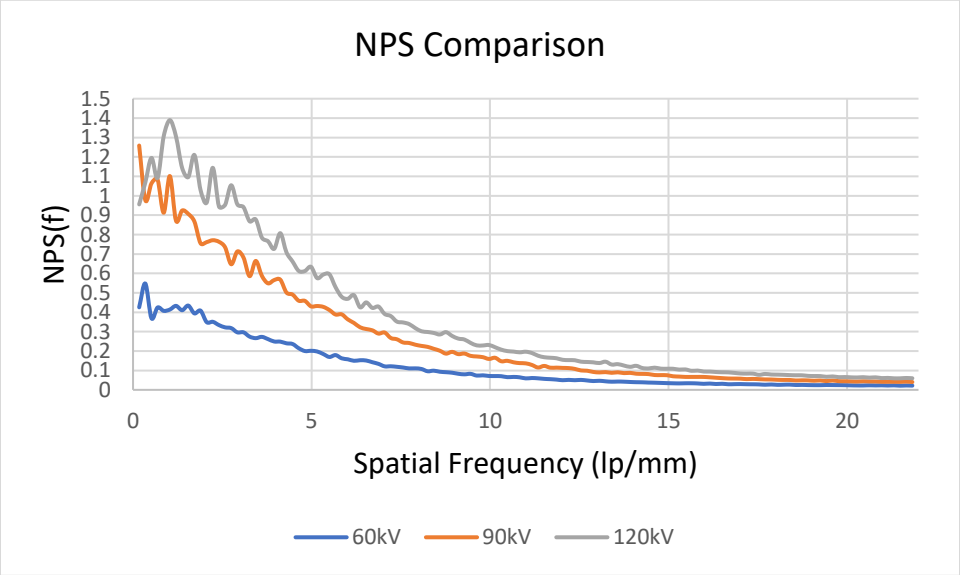

Figure 5 – 20. Comparison of the three NPS.

It is clear from Figure 5-20 that higher energy imaging yields larger noise variance. The DC effects seen near zero frequency also increase as energy increases. Since there is significant variation between noise power spectra, we can expect each one to impact the corresponding DQE significantly. The DQE results are presented in the next section.

5.4.4 DQE

The DQE results are presented below. Figures 5-21 through 5-22 provide the separate DQEs for 60kV, 90kV, and 120kV. It should be clear that the smaller NPS yields a higher DQE, while a larger NPS yields a lower DQE.

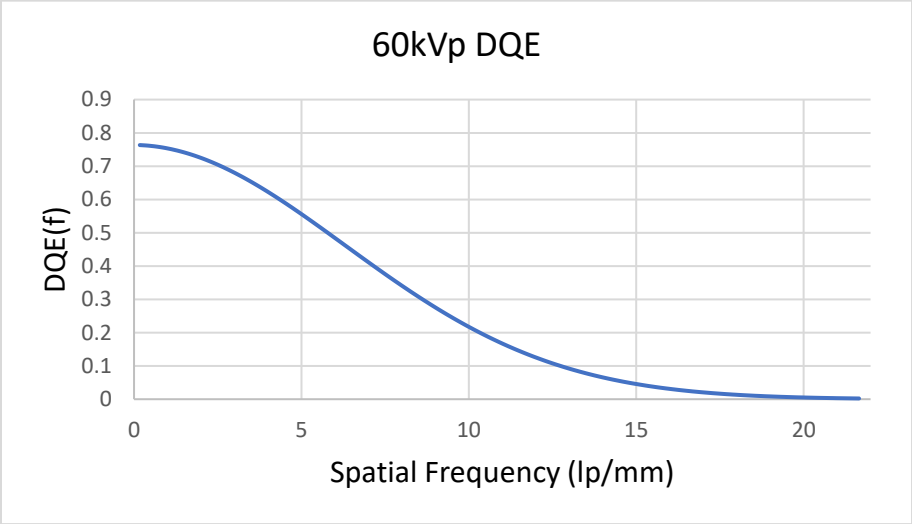

Figure 5 – 22. DQE at 60kV.

The 60kV DQE is clearly impacted by the lower, more slowly declining NPS. Since the higher energy NPS are larger and decline more steeply, we see in Figures 5-23 and 5-24 steeper DQE curves as well.

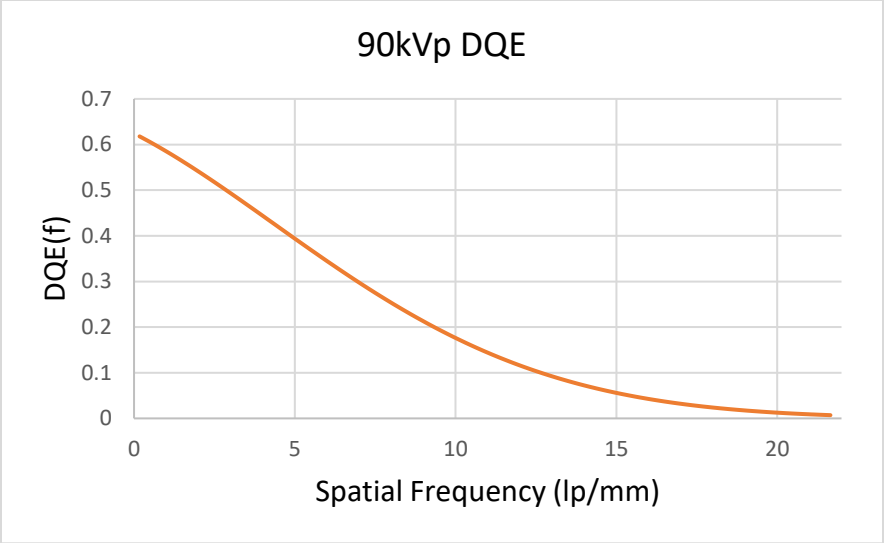

Figure 5 – 23. DQE at 90kV.

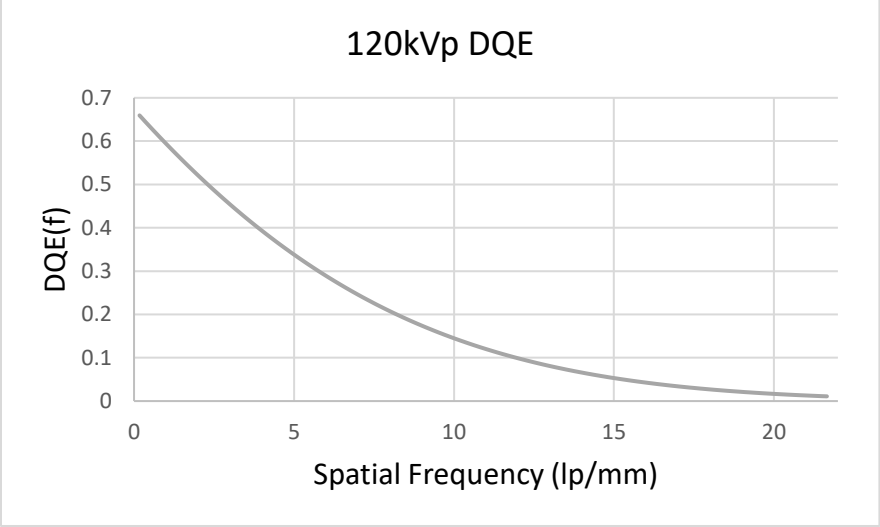

Figure 5 – 24. DQE at 120kV.

The above figures clearly show a sharper decline as the tube potential increases. When the three DQEs are plotted together, we see that the 60kV curve remains higher than the other, higher energies' curves until the cutoff frequency, where they converge. While theoretically the higher energy beam should see more high energy photons pass through the detector without contributing to the image, we see that the 120kV curve

begins with a higher DQE than that of 90kV. This can be explained by the DC component of the NPS curves, where strange spikes are present near zero frequency that do not match the overall trend. We also see in Figure 5-25 below that the 90kV curve quickly indicates a higher DQE than 120kV.

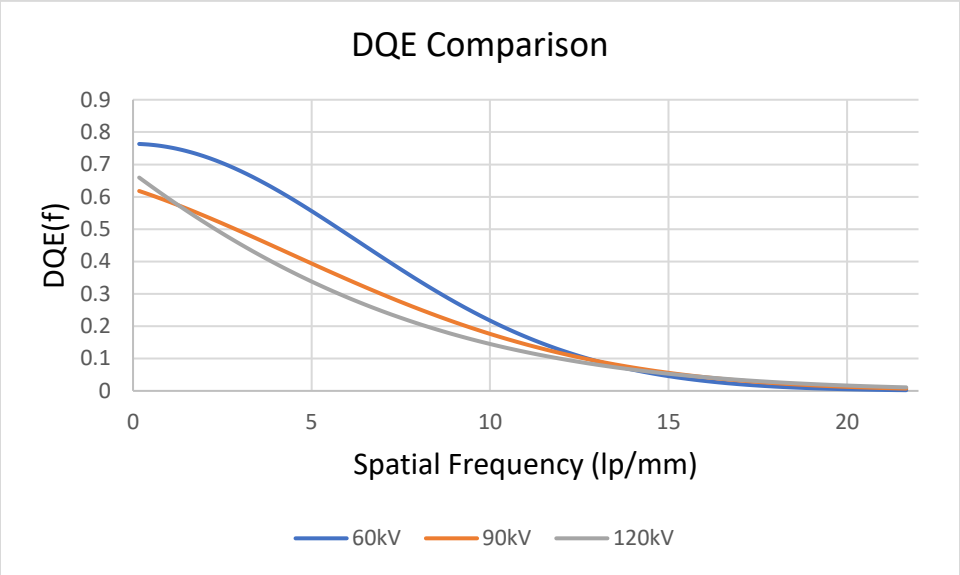

Figure 5 – 25. Comparison of DQE curves.

These results show promise in improving efficiency of the dose delivered to the patient when lowering the tube potential to mid-energy range. Further discussion is provided in the next chapter.

Chapter 6 Discussion and Conclusion

6.1 Summary of Study and Results

An in-line phase contrast prototype x-ray imaging system was characterized for imaging at 60kVp. The data from the 60kV images were compared to that of high energy image quality metrics, specifically 90kV and 120kV. Investigations included those into the MTF, Michelson contrast, NPS, and DQE of the prototype when operating at the described tube potentials. The MTFs for all three beam energies were approximately equivalent to each other, with a cutoff frequency of approximately 14 lp/mm. Michelson contrast data from angle resolution pattern images indicated that the cutoff frequency was approximately 14 lp/mm as well. The NPS results yielded significant variation due to the differing tube potentials, with the lowest energy beam yielding the smallest noise variance, while the highest energy beam yielded the largest variance. Data from the MTF and NPS data were used to calculate the DQE. The DQE data indicate that in-line phase contrast imaging can be more efficient than higher energy imaging of the same technique with the same radiation dose.

6.2 Future Research Directions

There are a few potential directions in which one can build upon this research in the future. Among them are optimization of imaging parameters, improvement of detectors and sources, and extension to three-dimensional imaging modalities such as tomosynthesis.

Further investigation is needed to determine the optimal imaging parameters for mid-energy phase contrast imaging. Since this is the first such investigation for this prototype, it is not known what the optimal magnification, SID, and SOD might be. Furthermore, the optimal material and thickness for the beam hardening filter are also unclear. It is possible that an Al filter with a thickness other than 1.2mm can see a more efficient usage of x-ray dose. Other materials may also be considered, such rhodium (Rh) and molybdenum (Mo), filters of which have been used in other investigations [79-81].

Other factors worth considering when optimizing the imaging system are the source and detector. The micro focus source used in this research can generate tube currents up to 300μA. Such low current results in fewer electrons being incident to the W target at any given moment, and therefore x-ray photons are emitted at a lower rate than other sources. To perform a diagnostic imaging procedure at the same dose as those conventionally used, a micro focus system will require a longer exposure time. There are other micro focus sources available which can generate somewhat higher current [82], but the improvement is minute. If micro focus sources were developed that could generate significantly higher current, any future medical imaging procedures using such sources would become much more time-efficient than they would be today.

Adjustments can also be made to the detector used in the prototype. The reason magnification was set to 2.2 for this research was the size of the detector's photodiode area. A magnification of 2.5 yielded an image of the object that was too large to be seen in its entirety by the detector. Increasing the size of the detector (i.e.

175mmx175mm photodiode area or larger) would increase the allowable magnification that can be used for research. Investigations can also be conducted into the efficacy of different kinds of detectors. As was previously stated, the detector used was manufactured with a scintillator consisting of GOS. Alternative materials may include cesium iodide (CsI), that has been doped with different elements such as sodium (Na) or thallium (Tl) [83]. Another research possibility is an investigation of the efficacy of a direct digital detector. The digital detector used in this research was "indirect," meaning that the scintillating layer converted the x-ray photons into visible light photons before converting the latter into electrons to be used in image generation. "Direct" detectors convert the x-ray photons immediately into electrons for image generation. Such investigations could lead to a more efficient imaging system.

Another opportunity to expand upon this research is in extending the characterization to three-dimensional imaging techniques such as breast tomosynthesis. Tomosynthesis is a technique similar to computed tomography (CT), though it uses less projection images. As in CT, multiple images are taken of the subject at different rotational orientations across a 180^{o} arc, though tomosynthesis makes use of a smaller arc [84-87]. The resulting projections are used to reconstruct a three-dimensional image [58]. One benefit of three-dimensional imaging is a reduction in structural noise, or the noise due to tissues within a body [58]. One challenge with two-dimensional imaging of a three-dimensional body is that there will inevitably be tissues overlapping each other regardless of the source and detector's orientation. Viewing the structures of a body in a three-dimensional will thus reduce some of the noise caused by tissues which do not

interest investigators. The technique is not without its tradeoffs, however. Naturally, any x-ray imaging procedure with multiple projections results in higher exposure to ionizing radiation for the patient. In techniques such as CT, which covers 180^{o} with many projections, the delivered dose will always be much higher than a single projection image. Tomosynthesis seeks to find an optimal balance between noise reduction and dose increase. Since it relies on fewer projections than CT, tomosynthesis will deliver less radiation to the patient, but will not reduce structural noise as much as CT [58].

Some research has investigated the feasibility of applying high energy in-line phase contrast imaging to tomosynthesis, with promising results [58, 88]. Assessing the same image quality metrics discussed in this thesis (MTF, NPS, and DQE) for mid-energy in-line phase contrast tomosynthesis would thus be a logical step forward from this research. Subjective investigations such as observer studies, in which images of specially designed phantoms (into which multiple features resembling different potentially cancerous lesions are placed) are scored by multiple viewers, will also prove important to any future investigation into tomosynthesis.

References

[1] M. Heron, "Deaths: Leading Causes for 2016," in "National Vital Statistics Reports," Centers for Disease Control and PreventionJuly 26, 2018 2018, vol. 67.

[2] R. L. Siegel, K. D. Miller, and A. Jemal, "Cancer statistics, 2019," *CA Cancer J Clin,* vol. 69, no. 1, pp. 7-34, Jan 2019.

[3] M. G. Marmot, D. G. Altman, D. A. Cameron, J. A. Dewar, S. G. Thompson, and M. Wilcox, "The benefits and harms of breast cancer screening: an independent review," *British Journal Of Cancer,* Report vol. 108, p. 2205, 06/06/online 2013.

[4] S. M. Friedewald *et al.*, "Breast Cancer Screening Using Tomosynthesis in Combination With Digital MammographyTomosynthesis and Mammography for Breast ScreeningTomosynthesis and Mammography for Breast Screening," *JAMA,* vol. 311, no. 24, pp. 2499-2507, 2014.

[5] R. Ballard-Barbash *et al.*, "Breast Cancer Surveillance Consortium: a national mammography screening and outcomes database," *AJR Am J Roentgenol,* vol. 169, no. 4, pp. 1001-8, Oct 1997.

[6] R. A. Smith, V. Cokkinides, and H. J. Eyre, "American Cancer Society Guidelines for the Early Detection of Cancer, 2003," *CA: A Cancer Journal for Clinicians,* vol. 53, no. 1, pp. 27-43, 2003.

[7] L. Tabar, G. Fagerberg, S. W. Duffy, and N. E. Day, "The Swedish two county trial of mammographic screening for breast cancer: recent results and calculation of benefit," *J Epidemiol Community Health,* vol. 43, no. 2, pp. 107-14, Jun 1989.

[8] L. Tabar *et al.*, "Efficacy of breast cancer screening by age. New results from the Swedish Two-County Trial," *Cancer,* vol. 75, no. 10, pp. 2507-17, May 15 1995.

[9] A. B. d. Gonzalez, "Risk of cancer from diagnostic X-rays: estimates for the UK and 14 other countries," *The lancet.,* vol. 363, no. 9406, p. 345, 2004.

[10] J. T. Bushberg, J. A. Seibert, E. M. Leidholt, and J. M. Boone, *The Essential Physics of Medical Imaging*, 3rd ed. Philadelphia, PA: Wolters Kluwer health/Lippincott Williams & Wilkins, 2012.

[11] P. C. Johns and M. J. Yaffe, "X-ray characterisation of normal and neoplastic breast tissues," *Phys Med Biol,* vol. 32, no. 6, pp. 675-95, Jun 1987.

[12] X. Wu, H. Liu, and A. Yan, "X-ray phase-attenuation duality and phase retrieval," *Opt Lett,* vol. 30, no. 4, pp. 379-81, Feb 15 2005.

[13] X. Wu and H. Liu, "A general theoretical formalism for X-ray phase contrast imaging," *J Xray Sci Technol,* vol. 11, no. 1, pp. 33-42, Jan 1 2003.

[14] D. Zhang, M. Donovan, L. L. Fajardo, A. Archer, X. Wu*, and H. Liu*, "Preliminary Feasibility Study of an In-line Phase Contrast X-Ray Imaging Prototype," *IEEE Transactions on Biomedical Engineering,* vol. 55, no. 9, pp. 2249-2257, 2008.

[15] X. Wu and H. Liu, "Clinical implementation of x-ray phase-contrast imaging: theoretical foundations and design considerations," *Med Phys,* vol. 30, no. 8, pp. 2169-79, Aug 2003.

[16] R. Fitzgerald, "Phase-sensitive x-ray imaging," *Physics today.,* vol. 53, no. 7, p. 23, 2000.

[17] S. Matsuo, T. Katafuchi, K. Tohyama, J. Morishita, K. Yamada, and H. Fujita, "Evaluation of edge effect due to phase contrast imaging for mammography," *Medical Physics,* vol. 32, no. 8, pp. 2690-2697, 2005.

[18] T. Tanaka *et al.*, "The first trial of phase contrast imaging for digital full-field mammography using a practical molybdenum x-ray tube," *Invest Radiol,* vol. 40, no. 7, pp. 385-96, Jul 2005.

[19] M. U. Ghani *et al.*, "Detectability comparison between a high energy x-ray phase sensitive and mammography systems in imaging phantoms with varying glandular-adipose ratios," *Phys Med Biol,* vol. 62, no. 9, pp. 3523-3538, May 7 2017.

[20] X. Wu and A. Yan, "Phase retrieval from one single phase contrast x-ray image," *Opt Express,* vol. 17, no. 13, pp. 11187-96, Jun 22 2009.

[21] X. Wu, "Robustness of a phase-retrieval approach based on phase-attenuation duality," *Journal of X-ray science and technology.,* vol. 15, no. 2, p. 85, 2007.

[22] E. Krestel, *Imaging Systems for Medical Diagnostics*. Germany: Siemens, 1980.

[23] Y. Guo, "Detectability Assessment of the High-energy X-ray In-line Phase Contrast Prototype for Dense Breasts," Master of Science, Electrical and Computer Engineering, University of Oklahoma, Norman, OK, 2018.

[24] A. Macovsky, *Medical Imaging Systems* (Information and Systems Science). Upper Saddle River, NJ: Prentice-Hall, Inc., 1983.

[25] J. H. Hubbell, "Photon mass attenuation and energy-absorption coefficients," *The International Journal of Applied Radiation and Isotopes,* vol. 33, no. 11, pp. 1269-1290, 1982/11/01/ 1982.

[26] C. Fedon *et al.*, "Dose and diagnostic performance comparison between phase-contrast mammography with synchrotron radiation and digital mammography: a clinical study report," *J Med Imaging (Bellingham),* vol. 5, no. 1, p. 013503, Jan 2018.

[27] X. Wu, M. D. Wong, A. E. Deans, and H. Liu, "X-ray Diagnostic Techniques," in *Biomedical Photonics Handbook*, T. Vo-Dinh, Ed. Tampa, FL: CRC Press, 2003.

[28] P. Zhu *et al.*, "Low-dose, simple, and fast grating-based X-ray phase-contrast imaging," *Proceedings of the National Academy of Sciences,* vol. 107, no. 31, pp. 13576-13581, 2010.

[29] I. Zanette *et al.*, "Speckle-Based X-Ray Phase-Contrast and Dark-Field Imaging with a Laboratory Source," *Physical Review Letters,* vol. 112, no. 25, p. 253903, 06/26/ 2014.

[30] U. Bonse and M. Hart, "AN X-RAY INTERFEROMETER," *Applied Physics Letters,* vol. 6, no. 8, pp. 155-156, 1965.

[31] E. D. Pisano *et al.*, "Human Breast Cancer Specimens: Diffraction-enhanced Imaging with Histologic Correlation—Improved Conspicuity of Lesion Detail Compared with Digital Radiography," *Radiology,* vol. 214, no. 3, pp. 895-901, 2000.

[32] D. Chapman *et al.*, "Diffraction enhanced x-ray imaging," *Physics in Medicine and Biology,* vol. 42, no. 11, pp. 2015-2025, 1997/11/01 1997.

[33] F. A. Dilmanian *et al.*, "Computed tomography of x-ray index of refraction using the diffraction enhanced imaging method," *Physics in Medicine and Biology,* vol. 45, no. 4, pp. 933-946, 2000/03/09 2000.

[34] J. Mollenhauer *et al.*, "Diffraction-enhanced X-ray imaging of articular cartilage," *Osteoarthritis and Cartilage,* vol. 10, no. 3, pp. 163-171, 2002/03/01/ 2002.

[35] A. Momose, "Recent Advances in X-ray Phase Imaging," *Japanese Journal of Applied Physics,* vol. 44, no. 9A, pp. 6355-6367, 2005/09/08 2005.

[36] F. Pfeiffer, T. Weitkamp, O. Bunk, and C. David, "Phase retrieval and differential phase-contrast imaging with low-brilliance X-ray sources," *Nature Physics,* vol. 2, no. 4, pp. 258-261, 2006/04/01 2006.

[37] Y. J. Liu *et al.*, "A new iterative algorithm to reconstruct the refractive index," *Physics in Medicine and Biology,* vol. 52, no. 12, pp. L5-L13, 2007/05/22 2007.

[38] R. Cerbino, L. Peverini, M. A. C. Potenza, A. Robert, P. Bösecke, and M. Giglio, "X-ray-scattering information obtained from near-field speckle," *Nature Physics,* Article vol. 4, p. 238, 01/20/online 2008.

[39] K. S. Morgan, D. M. Paganin, and K. K. W. Siu, "X-ray phase imaging with a paper analyzer," *Applied Physics Letters,* vol. 100, no. 12, p. 124102, 2012.

[40] S. Berujon, H. Wang, and K. Sawhney, "X-ray multimodal imaging using a random-phase object," *Physical Review A,* vol. 86, no. 6, p. 063813, 12/14/ 2012.

[41] D. Zhang, J. Rong, R. Chu, W. R. Chen, and H. Liu, "DQE measurements in magnification X-ray imaging," *Journal of X-ray science and technology,* vol. 14, pp. 141-150, 2006.

[42] D. Wu *et al.*, "Quantitative investigation of the edge enhancement in in-line phase contrast projections and tomosynthesis provided by distributing microbubbles on the interface between two tissues: a phantom study," *Physics in Medicine & Biology,* vol. 62, no. 24, pp. 9357-9376, 2017/11/21 2017.

[43] E. F. Donnelly, R. R. Price, and D. R. Pickens, "Quantification of the effect of system and object parameters on edge enhancement in phase-contrast radiography," *Medical Physics,* vol. 30, no. 11, pp. 2888-2896, 2003.

[44] A. Pogany, D. Gao, and S. W. Wilkins, "Contrast and resolution in imaging with a microfocus x-ray source," *Review of Scientific Instruments,* vol. 68, no. 7, pp. 2774-2782, 1997.

[45] D. Wu *et al.*, *Quantitative imaging of the microbubble concentrations by using an in-line phase contrast tomosynthesis prototype: a preliminary phantom study* (SPIE Medical Imaging). SPIE, 2016.

[46] D. Wu *et al.*, "Using Microbubble as Contrast Agent for High-Energy X-Ray In-line Phase Contrast Imaging: Demonstration and Comparison Study," (in eng), *IEEE transactions on bio-medical engineering,* vol. 65, no. 5, pp. 1117-1123, 2018/05// 2018.

[47] S. W. Wilkins, Y. I. Nesterets, T. E. Gureyev, S. C. Mayo, A. Pogany, and A. W. Stevenson, "On the evolution and relative merits of hard X-ray phase-contrast imaging methods," *Philos Trans A Math Phys Eng Sci,* vol. 372, no. 2010, p. 20130021, Mar 6 2014.

[48] F. Arfelli *et al.*, "Mammography with Synchrotron Radiation: Phase-Detection Techniques," *Radiology,* vol. 215, no. 1, pp. 286-293, 2000.

[49] S. W. Wilkins, T. E. Gureyev, D. Gao, A. Pogany, and A. W. Stevenson, "Phase-contrast imaging using polychromatic hard X-rays," *Nature,* vol. 384, no. 6607, pp. 335-338, 1996/11/01 1996.

[50] X. Wu and H. Liu, "Phase-space evolution of x-ray coherence in phase-sensitive imaging," *Appl Opt,* vol. 47, no. 22, pp. E44-52, Aug 1 2008.

[51] M. U. Ghani *et al.*, "Impact of a single distance phase retrieval algorithm on spatial resolution in X-ray inline phase sensitive imaging," *Biomedical Spectroscopy and Imaging,* pp. 1-12, 2019.

[52] X. Wu and H. Liu, "A dual detector approach for X-ray attenuation and phase imaging," *Journal of X-ray science and technology,* vol. 12, no. 1, pp. 35-42, 2004.

[53] A. Yan, X. Wu, and H. Liu, "An attenuation-partition based iterative phase retrieval algorithm for in-line phase-contrast imaging," *Optics Express,* vol. 16, no. 17, pp. 13330-13341, 2008/08/18 2008.

[54] X. Wu and H. Liu, "X-Ray cone-beam phase tomography formulas based on phase-attenuation duality," *Opt Express,* vol. 13, no. 16, pp. 6000-14, Aug 8 2005.

[55] F. Meng, H. Liu, and X. Wu, "An iterative phase retrieval algorithm for in-line x-ray phase imaging," *Opt Express,* vol. 15, no. 13, pp. 8383-90, Jun 25 2007.

[56] F. Meng, H. Liu, and X. Wu, "Feasibility study of the iterative x-ray phase retrieval algorithm," *Appl Opt,* vol. 48, no. 1, pp. 91-8, Jan 1 2009.

[57] M. D. Wong *et al.*, "Dose and detectability improvements with high energy phase sensitive x-ray imaging in comparison to low energy conventional imaging," *Physics in Medicine and Biology,* vol. 59, no. 9, pp. N37-N48, 2014/04/15 2014.

[58] D. Wu *et al.*, "Characterization of a high-energy in-line phase contrast tomosynthesis prototype," *Medical Physics,* vol. 42, no. 5, pp. 2404-2420, 2015.

[59] F. Ouandji, E. Potter, W. R. Chen, Y. Li, D. Tang, and H. Liu, "Characterization of a CCD-based digital x-ray imaging system for small-animal studies: properties of spatial resolution," *Appl Opt,* vol. 41, no. 13, pp. 2420-7, May 1 2002.

[60] M. Donovan, D. Zhang, and H. Liu, "Step by step analysis toward optimal MTF algorithm using an edge test device," *J Xray Sci Technol,* vol. 17, no. 1, pp. 1-15, 2009.

[61] H. Fujita *et al.*, "A simple method for determining the modulation transfer function in digital radiography," *IEEE Transactions on Medical Imaging,* vol. 11, no. 1, pp. 34-39, 1992.

[62] E. Buhr, S. Guenther-Kohfahl, and U. Neitzel, *Simple method for modulation transfer function determination of digital imaging detectors from edge images* (Medical Imaging 2003). SPIE, 2003.

[63] M. U. Ghani *et al.*, "Investigation of spatial resolution characteristics of an in vivo microcomputed tomography system," *Nuclear Instruments and Methods in Physics Research Section A: Accelerators, Spectrometers, Detectors and Associated Equipment,* vol. 807, pp. 129-136, 2016/01/21/ 2016.

[64] B. Zhao and W. Zhao, "Imaging performance of an amorphous selenium digital mammography detector in a breast tomosynthesis system," *Med Phys,* vol. 35, no. 5, pp. 1978-87, May 2008.

[65] P. L. Smith, "New Technique for Estimating the MTF of an Imaging System from its Edge Response," *Appl Opt,* vol. 11, no. 6, p. 1424, Jun 1 1972.

[66] B. Tatian, "Method for Obtaining the Transfer Function from the Edge Response Function," *Journal of the Optical Society of America,* vol. 55, no. 8, pp. 1014-1019, 1965/08/01 1965.

[67] J. M. Boone, "Determination of the presampled MTF in computed tomography," *Medical Physics,* vol. 28, no. 3, pp. 356-360, 2001.

[68] C. C. Shaw, X. Liu, M. R. Lemacks, J. X. Rong, and G. J. Whitman, *Optimization of MTF and DQE in magnification radiography: a theoretical analysis* (Medical Imaging 2000). SPIE, 2000.

[69] H. Schiabel, A. F. Frere, and P. M. Marques, "The modulation transfer function. A simplified procedure for computer-aided quality evaluation in mammography," *IEEE Eng Med Biol Mag,* vol. 16, no. 4, pp. 93-101, Jul-Aug 1997.

[70] J. T. Dobbins III, E. Samei, N. T. Ranger, and Y. Chen, "Intercomparison of methods for image quality characterization. II. Noise power spectruma)," *Medical Physics,* vol. 33, no. 5, p. 1454, 2006.

[71] J. Hangyi, W. R. Chen, and L. Hong, "Techniques to improve the accuracy and to reduce the variance in noise power spectrum measurement," *IEEE Transactions on Biomedical Engineering,* vol. 49, no. 11, pp. 1270-1278, 2002.

[72] D. Zhang, H. Liu, and X. Wu, "DQE analysis on a dual detector phase x-ray imaging system," *Physics in Medicine and Biology,* vol. 53, no. 18, pp. 5165-5176, 2008/08/22 2008.

[73] A. D. A. Maidment and M. J. Yaffe, "Analysis of the spatial-frequency-dependent DQE of optically coupled digital mammography detectors," *Medical Physics,* vol. 21, no. 6, pp. 721-729, 1994.

[74] D. Zhang *et al.*, "Impact of Additive Noise on System Performance of a Digital X-ray Imaging System," *IEEE Transactions on Biomedical Engineering,* vol. 54, no. 1, pp. 69-73, 2007.

[75] M. J. Yaffe and J. A. Rowlands, "X-ray detectors for digital radiography," *Phys Med Biol,* vol. 42, no. 1, pp. 1-39, Jan 1997.

[76] M. U. Ghani *et al.*, "Characterization of Continuous and Pulsed Emission modes of a Hybrid Micro Focus X-ray Source for Medical Imaging Applications," (in eng), *Nuclear instruments & methods in physics research. Section A, Accelerators, spectrometers, detectors and associated equipment,* vol. 853, pp. 70-77, 2017.

[77] M. Wong, D. Zhang, J. Rong, X. Wu, and H. Liu, "Optimizing photon fluence measurements for the accurate determination of detective quantum efficiency," *Journal of Electronic Imaging,* vol. 18, no. 4, pp. 1-9, 9, 2009.

[78] J. M. Boone and J. A. Seibert, "An accurate method for computer-generating tungsten anode x-ray spectra from 30 to 140 kV," *Med Phys,* vol. 24, no. 11, pp. 1661-70, Nov 1997.

[79] F. Meng, A. Yan, G. Zhou, X. Wu, and H. Liu, "Development of a dual-detector X-ray imaging system for phase retrieval study," *Nuclear Instruments and Methods in Physics Research Section B: Beam Interactions with Materials and Atoms,* vol. 254, no. 2, pp. 300-306, 2007/01/01/ 2007.

[80] M. U. Ghani *et al.*, "Low dose high energy x-ray in-line phase sensitive imaging prototype: Investigation of optimal geometric conditions and design parameters," *J Xray Sci Technol,* vol. 23, no. 6, pp. 667-82, 2015.

[81] X. Wu, H. Liu, and A. Yan, "Optimization of X-ray phase-contrast imaging based on in-line holography," *Nuclear Instruments and Methods in Physics Research Section B: Beam Interactions with Materials and Atoms,* vol. 234, no. 4, pp. 563-572, 2005/07/01/ 2005.

[82] M. Ghani, "Optimization of a High Energy X-ray Inline Phase Sensitive Imaging System for Diagnosis of Breast Cancer," Ph.D. Doctoral Dissertation, Electrical and Computer Engineering, University of Oklahoma, Norman, OK, 2018.

[83] Y. El-Mohri *et al.*, "Performance of a high fill factor, indirect detection prototype flat-panel imager for mammography," *Medical Physics,* vol. 34, no. 1, pp. 315-327, 2007.

[84] H. Miao, X. Wu, H. Zhao, and H. Liu, "A phantom-based calibration method for digital x-ray tomosynthesis," (in eng), *Journal of X-ray science and technology,* vol. 20, no. 1, pp. 17-29, 2012.

[85] D. Wu, H. Miao, Y. Li, X. Wu, and H. Liu, *In-plane spatial resolution measurements of a phase-contrast tomosynthesis prototype* (SPIE BiOS). SPIE, 2012.

[86] D. Wu *et al.*, *A phantom study to characterize the imaging quality of a phase-contrast tomosynthesis prototype* (SPIE BiOS). SPIE, 2013.

[87] M. U. Ghani *et al.*, *Quantitative comparison of spatial resolution in step-and-shoot and continuous motion digital breast tomosynthesis* (SPIE Medical Imaging). SPIE, 2016.

[88] M. U. Ghani *et al.*, "Detectability comparison of simulated tumors in digital breast tomosynthesis using high-energy X-ray inline phase sensitive and commercial imaging systems," (in eng), *Physica medica : PM : an international journal devoted to the applications of physics to medicine and biology : official journal of the Italian Association of Biomedical Physics (AIFB),* vol. 47, pp. 34-41, 2018/03// 2018.